

Equatorial Mountain Torques and Cold Surges Preconditioning

SYLVAIN MAILLER

Laboratoire de Météorologie Dynamique du CNRS, Paris, France

École Nationale des Ponts et Chaussées, Marne la Vallée, France

FRANÇOIS LOTT *

Laboratoire de Météorologie Dynamique du CNRS, Paris, France

* *Corresponding author address:* François Lott, Laboratoire de Météorologie Dynamique,

Ecole Normale Supérieure, 24, rue Lhomond, 75231 PARIS cedex 05, France

E-mail: flott@lmd.ens.fr

ABSTRACT

The evolution of the two components of the Equatorial Mountain Torque (EMT) applied by mountains on the atmosphere is analyzed in the NCEP reanalysis. A strong lagged relationship between the EMT component along the Greenwich axis (T_{M1}) and the EMT component along the 90°E axis (T_{M2}) is found, with a pronounced signal on T_{M1} followed by a signal of opposite sign on T_{M2} . It is shown that this result holds for the major massifs (Antarctica, Tibetan Plateau, the Rockies and the Andes) if a suitable axis system is used for each of them. For the midlatitude mountains, this relationship is in part associated with the development of the cold surges.

Following these results, we make the two hypothesis that the mountain forcing on the atmosphere is well measured by the regional EMTs, and that this forcing partly drives the cold surges. To support this, a purely dynamical linear model is proposed. This model is written on the sphere but using a f-plane quasi-geostrophic approximation and only includes the mountain forcings. In this model, a positive (resp. negative) peak in T_{M1} produced by a mountain massif in the northern (resp. southern) hemisphere is due to a large scale high surface pressure anomaly poleward of the massif. At a later stage, high pressure and low temperature anomalies develop in the lower troposphere east of the mountain, explaining the signal on T_{M2} and providing the favorable conditions for the cold surges development.

It is concluded that the EMT is a good measure of the dynamical forcing of the atmospheric flow by the mountains and that the poleward forces exerted by mountains on the atmosphere are substantial drivers of the cold surges, at least in their early stage. Therefore, the EMT time series can be important diagnostics to assess the representation of mountains in General Circulation Models.

1. Introduction

The influence of the mountains on meteorology is a problem of long standing interest. At the synoptic scales, this interest is due to the fact that mountains can help the development of cyclones in their lee side, or induce cold surges that can travel equatorward along the eastern mountain flanks. The problem of lee cyclogenesis was studied extensively in the 80s and 90s. It has been documented in case studies (e.g. Buzzi and Tibaldi 1978; Clark 1990), numerical studies (Egger 1988), and partly explained by theoretical models (Pierrehumbert 1985; Smith 1984, 1986; Speranza et al. 1985). The cold surges are a growing topic of interest because they are an important source of atmospheric variability in winter along the eastern flanks of the major mountain ranges (Hsu and Wallace 1985). They are also relevant for the global climate because they connect the meteorology of the midlatitudes to the tropical one (Garreaud 2001; Chen et al. 2004). As an illustration of this, the east-asian cold surges interact with the winter monsoon over eastern Asia, the South China Sea, the Maritime Continent, and even the Bay of Bengal (Chang et al. 1979; Chang and Lau 1980; Slingo 1998; Tangang et al. 2008; Mailler and Lott 2009).

In mountain meteorology, it is quite common to measure the dynamical influence of mountains on the atmosphere by forces (e.g. Davies and Phillips 1985; Bessemoulin et al. 1993). In this approach, there is a distinction between the drag forces that are opposed to the winds at low level and the lift forces that are perpendicular to them. At the mesoscales, where the mountain flow dynamics is controlled by gravity waves and include low level flow blocking, the drag force is very important, while at the synoptic and planetary scales, the lift force plays a key role and causes vortex compression over mountains (Smith 1979). By

triggering baroclinic wave development and forcing planetary scale waves, these lift forces have an impact on the large-scale atmospheric flow and their proper representation in GCMs is an important issue (Lott 1999).

If we adopt a planetary scale approach, which is mandatory for large-scale mountains, the Atmospheric Angular Momentum (AAM) budget (Feldstein 2006) provides a more satisfactory formalism to analyze these forces, with the mountain forces translating into torques along the three planetary axes. For example, Mailler and Lott (2009) have shown that before convective events associated with the east-asian winter monsoon, there are strong signals on the Equatorial Mountain Torque (EMT) components T_{M1} and T_{M2} due to the Tibetan Plateau (hereinafter TP). In agreement with other authors (Egger et al. (2007), Egger and Hoinka (2008)), they also show that the positive torques along the Greenwich axis are due to a positive surface pressure anomaly to the North of the TP, while the negative torques along the 90°E axis are due to a positive pressure anomaly along its eastern slopes (see Fig. 1 where it is also illustrated how a mountain force \mathbf{F} translates into torques along the equatorial axes).

In the past, the analysis of the mountain torques was mainly focused on the changes it induces on the Atmospheric Angular Momentum and essentially to interpret the changes in the Earth Orientation Parameters (e.g. Rosen and Salstein 1983). In this context, the axial mountain torque T_{M3} has been analyzed by many authors, with among others, Iskenderian and Salstein (1998) relating the variations of T_{M3} to the midlatitudes dynamics at synoptic scales and Weickmann and Sardeshmukh (1994) relating its variations to the tropical dynamics at intraseasonal time scales. The two representative studies cited above are only focused on the axial mountain torque T_{M3} . The two components of the EMT have received

less attention, with Feldstein (2006) analyzing their relation with the changes in the equatorial components of the Atmospheric Angular Momentum, and Egger and Hoinka (2008) investigating the regional circulation patterns associated to the equatorial torques produced by the TP.

On top of these issues, the axial mountain torque can be used to measure the dynamical influence of the mountains on the weather and on the climate. It is in this context that Lott et al. (2004) found that T_{M3} produces changes in the Arctic Oscillation at periodicities below 30 days. Their results, based on diagnostics from the NCEP-NCAR reanalysis, have been confirmed using a GCM (Lott et al. 2005), and explained by a simple comprehensive model (Lott and d'Andrea 2005).

Following these lines of work, the purpose of this paper is to show that the temporal evolution of the two components of the EMT is related to the dynamical forcing of the cold surges by the major midlatitude mountain ranges. An emphasis will be given to the TP and to the east-asian cold surges but the case of the Rockies and the Andes will also be discussed. To establish the link between the EMT and the cold surges, we will use two pieces of independent evidence. The first is based on a statistical analysis of the NCEP reanalysis data, where the two components of the EMT are evaluated globally and for each major mountain range separately. The temporal evolution of the surface patterns of pressure and temperature associated to the two EMT components are then analyzed and compared to those occurring during cold surges. The second is based on a analytical model that gives a comprehensive explanation for the relationship between the EMT components and the cold surges. This model is purely dynamical and only retains two essential features of the cold surge dynamics : the cold surges are related to low level cold advection from the midlatitudes

to the tropics, and they are preceded by high pressure anomalies poleward of the mountain massif. Because of its simplicity, this model is only used to show that mountain forcings yielding to EMTs with amplitudes comparable with those observed, are largely sufficient to trigger the initial phase of cold surges.

The plan of the paper is as follows. Section 2 presents the statistical analysis. From the NCEP-NCAR reanalysis, we evaluate the two components of the EMT globally and for each major mountain range. For the Rockies, the Andes and the TP, we then perform a composite analysis of the surface fields keyed to the EMT. Section 3 presents the theoretical model and our interpretation for the relation between the mountain forcing and the EMTs. Section 4 uses the model results to interpret the observational results of section 2. Section 5 summarizes and discusses the significance of our results for (i) the cold surges preconditioning, (ii) the Equatorial Atmospheric Angular Momentum Budget, and (iii) the representation of mountains in GCMs.

2. Statistical analysis

Our data are taken from the NCEP-NCAR reanalysis (Kalnay et al. 1996) products for the 1979-2007 period. Specifically, we use the surface pressure, P_S , the .995 sigma level temperature, T_{50m} , and the surface elevation, h . We will also use the tridimensional fields of zonal wind u and temperature T . To focus on the subseasonal variability, we will remove the annual cycle when needed. This is done by subtracting the daily climatology obtained by averaging over the 29 years of our data set. When used, those subseasonal data will be identified by a tilde symbol, for instance the subseasonal surface pressure will be written \tilde{P}_s .

a. Spectral analysis of the Equatorial Mountain Torques

The two components of the global subseasonal EMT acting on the atmosphere are computed following Feldstein (2006):

$$\tilde{T}_{M1}(t) = -a^2 \iint_{\phi, \lambda} h(\lambda, \phi) \left(-\sin \lambda \cos \phi \frac{\partial \tilde{P}_s}{\partial \phi} + \cos \lambda \sin \phi \frac{\partial \tilde{P}_s}{\partial \lambda} \right) d\phi d\lambda, \quad (1a)$$

$$\tilde{T}_{M2}(t) = -a^2 \iint_{\phi, \lambda} h(\lambda, \phi) \left(\cos \lambda \cos \phi \frac{\partial \tilde{P}_s}{\partial \phi} + \sin \lambda \sin \phi \frac{\partial \tilde{P}_s}{\partial \lambda} \right) d\phi d\lambda, \quad (1b)$$

where a , ϕ , and λ are the Earth radius, the latitude, and the longitude respectively. In (1), \tilde{T}_{M1} is the component of the EMT along the equatorial axis which is at 0° longitude (the Greenwich axis) and \tilde{T}_{M2} is the component along the equatorial axis at 90°E . Following Egger and Hoinka (2000), we will express all the torques in Hadley (Ha), with $1 \text{ Ha} = 10^{18} \text{ kg m}^2 \text{ s}^{-2}$.

The individual contributions of the major mountain ranges (here the TP, the Rockies, the Andes, Antarctica and Greenland) to the EMT can be computed by restricting the integrations in (1) to sectors including the considered mountain range and which are given in Table (1). Nevertheless, to compare the dynamics associated with the EMT produced by these mountains, the fact that they are located at different places has to be taken into account. For instance, the fact that a northward force applied to the atmosphere around the central location of the TP will mainly result in a positive \tilde{T}_{M1} (and a small \tilde{T}_{M2}) is due fact that the TP is centered around the latitude 90°E (Table (1)). In the following we will note this latitude λ_{TP} , and note λ_X and ϕ_X the longitude and the latitude of the center of mass of the mountain massif X (with $X = \text{TP, R, Ad, At, and G}$ for the TP, the Rockies, the Andes, Antarctica, and Greenland respectively). More precisely, they are the longitude

and latitude of the vector

$$\mathbf{r}_X = \frac{\int_{\lambda_{1X}}^{\lambda_{2X}} \int_{\phi_{1X}}^{\phi_{2X}} h(\lambda, \phi) \mathbf{r}(\lambda, \phi) \cos \phi d\phi d\lambda}{\int_{\lambda_{1x}}^{\lambda_{2x}} \int_{\phi_{1x}}^{\phi_{2x}} h(\lambda, \phi) \cos \phi d\phi d\lambda} \quad (2)$$

where $\mathbf{r}(\lambda, \phi) = a (\cos \lambda \cos \phi, \sin \lambda \cos \phi, \sin \phi)$, and where λ_{1X} , λ_{2X} , ϕ_{1X} , and ϕ_{2X} are the limits given in Table (1), where are also given the λ_X s and the ϕ_X s resulting from (2).

To make the results for different mountains comparable, the local equatorial torques for a mountain range X will be computed along equatorial axes that are rotated by $\lambda_X - \pi/2$, which means that the second equatorial axis is now at the longitude λ_X of the mountain considered. As said before this rotation is not needed for the TP, and is not adapted for Antarctica, which covers all the longitudes. In the following, the subseasonal regional contributions to the EMTs expressed in these rotated axis will be noted $(\tilde{T}_{X1}; \tilde{T}_{X2})$ where X is the name of the corresponding mountain massif. As an illustration, $\tilde{T}_{X1} = 0$ and $\tilde{T}_{X2} > 0$ means that the contribution of the massif X to the EMT vector is oriented along the longitude λ_X . The variance of each of the contributions is given in Tab. 2, indicating that, while Antarctica is the strongest single contributor, the midlatitude massifs can have a significant impact at least during the northern hemisphere winter.

To characterize the coherence and phase relationship between the two components of the global EMT, we next perform a conventional cross-spectral analysis between the corresponding series (Fig. 2, see caption for details on the method). The cospectrum between \tilde{T}_{M1} and \tilde{T}_{M2} in Fig. 2a shows that the two torques are significantly related with each other for periodicities between 2 and 20 days, a spectral domain that contains most of the variance of \tilde{T}_{M1} and \tilde{T}_{M2} (see Fig. 2cd). The phase in Fig. 2b of nearly $\frac{\pi}{2}$ shows that \tilde{T}_{M1} and \tilde{T}_{M2} are close to being in quadrature, with the EMT vector rotating westward.

The same analysis applied to the rotated EMTs associated with the individual mountains (Fig. 3) shows that for the Andes, the Rockies, the TP and Antarctica, \tilde{T}_{X1} and \tilde{T}_{X2} are close to being in quadrature as well (Fig. 3), which means that the regional EMT vectors also rotate westward. These results are consistent with those in Egger and Hoinka (2008) who considered the TP only and used lagged correlations rather than a spectral analysis.

The fact that all the regional EMT vectors (except Greenland, not shown) rotate westward like the global EMT indicates that the global behavior of the EMT is in part the result of regional circulations, the global EMT vector being the sum of all the regional contributions.

b. Regional circulation patterns

One of the central points we wish to make is that when a high pressure anomaly is located poleward of a given mountain massif X (X=TP, R or Ad) in the northern (resp. southern) midlatitudes, it gives rise to a positive (resp. negative) mountain torque \tilde{T}_{X1} , and that this mountain torque in part controls the future evolution of the flow, triggering a cold surge and a negative (resp. positive) \tilde{T}_{X2} . To support this picture observationally, composites will be built for the surface fields keyed to the positive peaks of \tilde{T}_{TP1} and \tilde{T}_{R1} , and to the negative peaks of \tilde{T}_{Ad1} .

In the following, the time lags are expressed in days relative to the peaks in \tilde{T}_{X1} : D0 is the day when \tilde{T}_{X1} peaks, D-2 is two days before, and D+2 is two days after. For instance, in the case of the TP at D0, the composite is the average of the values found for the days when \tilde{T}_{TP1} exceeds a given positive threshold. The threshold is chosen in order that 20 positive

peaks in \tilde{T}_{TP1} are selected, and we impose a 20 days gap between the dates selected. This last restriction, which ensures a statistical independence between the dates selected, allows to use a Student t-test to evaluate the confidence levels. At $D+l$ (resp. $D-l$), the composite is built with the values corresponding to the dates situated at the lag l days after (resp. before) the 20 positive peaks identified above.

Figure 4 shows the composites of \tilde{T}_{X2} keyed to \tilde{T}_{X1} for the TP, the Rockies and the Andes. In it, we see that for these three massifs, the peaks in \tilde{T}_{X1} are followed by peaks the opposite sign in \tilde{T}_{X2} . Note that a less significant signal in \tilde{T}_{X2} of the same sign as \tilde{T}_{X1} tends to precede. This result is consistent with the cross-spectral analysis in Fig. 3a-c with \tilde{T}_{X1} and \tilde{T}_{X2} in quadrature, but provides the additional information that the signal in \tilde{T}_{X2} is larger after than before the peaks in \tilde{T}_{X1} . This is a first indicator that \tilde{T}_{X1} contributes to the establishment of \tilde{T}_{X2} at a later stage. From a more global viewpoint we have also analysed the composites of the global EMT to the regional ones. In agreement with the results in Tab. 2 we found that the peaks in the EMTs due to the Rockies and the TP are related to significant signal on both components of the global EMT.

1) TIBETAN PLATEAU

The composites of \tilde{P}_S and \tilde{T}_{50m} keyed on the maxima of \tilde{T}_{TP1} in Fig. 5 show that the anomalies of \tilde{T}_{TP1} and \tilde{T}_{TP2} are linked to the clockwise movement of cold temperature and high pressure anomalies around the TP, from Siberia to eastern China. This movement begins at $D-2$ (Fig. 5ab) with the formation of high pressure and low temperature anomalies centered in western Siberia, later strengthening and moving to central Siberia at $D0$ (Fig. 5cd). These

anomalies are strong (16 hPa and 10 K) and largely significant. The strong anomaly of surface pressure north of the TP at D0 corresponds to the situation presented in Fig. 1a and explains the peak of \tilde{T}_{TP1} at that time (Fig. 4a).

At D+2, the surface pressure and surface temperature anomalies have shifted to eastern China (Fig. 5ef). At this time, the pressure gradient across the TP is mostly in the zonal direction, corresponding to the schematic picture in Fig. 1b, and this induces a negative \tilde{T}_{TP2} (Fig. 4a). The surface pressure and surface temperature patterns at that time (Fig. 5ef) are strongly reminiscent of the east-asian cold surges (see Fig. 7 of Zhang et al. (1997)). Finally, at D+4, the anomaly in surface pressure weakens and moves towards the South China Sea. The anomaly in surface temperature remains strong (7 K in southeastern China) and moves to the tropics (up to 4 K in the northern part of the South China sea), as occurs at the end of the life cycle of a cold surge (Zhang et al. (1997)). It is worth noting that the anomalies that are associated to peaks in \tilde{T}_{TP1} begin their life cycle in the Siberian midlatitudes and finish it 4 to 6 days later in tropical East-Asia.

2) ROCKIES

The composites of \tilde{P}_S and \tilde{T}_{50m} keyed on the maxima of \tilde{T}_{R1} are shown on Fig. 6. These composites are quite similar to those for the TP in Fig. 5: anomalies of high \tilde{P}_S and low \tilde{T}_{50m} are located over Alaska and the Arctic ocean at D-2 (Fig. 6ab), and move to the Canadian plains at D0 (Fig. 6cd), being very strong at this time (22 hPa and 12 K at D0). At D+2 (Fig. 6ef), they stretch southeastward along the eastern flank of the Rockies, covering the Gulf of Mexico and a part of central America. The anomalies displayed at that time are very

similar to the structure of the North-american cold surges, with cold air masses traveling southward from Canada to the Gulf of Mexico (Colle and Mass (1995)) and occasionally reaching the Eastern Pacific across Central America (Schultz et al. (1997))). At D+4 and after, the composites lose significance more rapidly than in the case of the TP (not shown). The shift of the high pressure anomaly from the northwestern slopes of the Rockies to their eastern slopes between D-2 and D+2 explains that \tilde{T}_{R2} shifts from positive to negative values during this period (Fig. 4b).

3) ANDES

The composites of \tilde{P}_S and \tilde{T}_{50m} keyed on the minima of \tilde{T}_{Ad1} are in Fig. 7. At D-2 (Fig. 7a), a high pressure system is arriving from the Pacific to the southern tip of the Andes. At D0 in Fig. 7cd, this anticyclone begins to interact substantially with the Andes, with a strong ridge building up along the eastern flank of the mountains. This ridge is associated with a cold anomaly extending meridionally from 50°S to 20°S along the eastern flank of the Andes. At D+2 the signal on the eastern flank of the Andes becomes even more pronounced (reaching 10 hPa and -10 K around 25°S). These strong anomalies at subtropical latitudes are quite remarkable and correspond to the ones generated by the south-american cold surges (Seluchi and Nery (1992); Marengo et al. (1997); Garreaud (2000)), suggesting that negative events on \tilde{T}_{Ad1} are an important factor in the generation of these events. Similarly to what happens in the case of the TP (Fig. 5), the low temperature and high surface pressure anomaly have moved further into the tropics at D+4 (Fig. 7g), being significant as far north as 5°N. The evolution of the surface pressure patterns explains the evolution of the

composite \tilde{T}_{Ad2} as shown in Fig. 4c: \tilde{T}_{Ad2} has a negative peak at D-2 when the high pressure arrives from the Pacific ocean and reaches the western slopes of the Andes (Fig.7a), then \tilde{T}_{Ad2} has a positive tendency at D0 due to the ridge formation along the eastern mountain slopes (Fig. 7c), and reaches strong positive values at D+1 and D+2 when the ridge further strengthens and moves northward along the mountain (Fig. 7e).

3. Theoretical model

a. basic equations

To interpret the temporal evolution of the EMT vector and its relation with the surface fields discussed in section 2, we will next use a linear model based on the quasi-geostrophic f -plane approximation of the anelastic Equations on the sphere. In this model, we will impose a background zonal geostrophic wind $\bar{u}_g(\phi, z)$ in thermal wind balance with a background potential temperature $\bar{\theta}(\phi, z)$,

$$f\bar{u}_{gz} = \frac{g}{a\theta_0}\bar{\theta}_\phi \quad (3)$$

with the Coriolis parameter $f = 2\Omega \sin \phi_r$, where ϕ_r is a constant reference latitude. Still in (3), $\theta_0(z)$ is a background potential temperature corresponding to the atmosphere at rest.

In this linear framework, the equations for the disturbance produced by the mountain are

$$\left(\frac{\partial}{\partial t} + \frac{\bar{u}_g}{a \cos \phi} \frac{\partial}{\partial \lambda}\right) u'_g + \frac{(\bar{u}_g \cos \phi)_\phi}{a \cos \phi} v'_g - f v' = -\frac{1}{a \cos \phi} \frac{\partial \Phi'}{\partial \lambda} \quad (4a)$$

$$\left(\frac{\partial}{\partial t} + \frac{\bar{u}_g}{a \cos \phi} \frac{\partial}{\partial \lambda}\right) v'_g + 2 \frac{\bar{u}_g u'_g}{a} \tan \phi + f u' = -\frac{1}{a} \frac{\partial \Phi'}{\partial \phi} + \frac{F'}{\rho_r} \delta(z) \quad (4b)$$

$$\frac{\partial \Phi'}{\partial z} - g \frac{\theta'}{\theta_0} = 0 \quad (4c)$$

$$\frac{\rho_0}{a \cos \phi} \left(\frac{\partial u'}{\partial \lambda} + \frac{\partial v' \cos \phi}{\partial \phi}\right) + \frac{\partial \rho_0 w'}{\partial z} = 0 \quad (4d)$$

$$\left(\frac{\partial}{\partial t} + \frac{\bar{u}_g}{a \cos \phi} \frac{\partial}{\partial \lambda}\right) \theta' + \frac{\bar{\theta}_\phi}{a} v'_g + \frac{d\theta_0}{dz} w' = Q'(\lambda, \phi) \frac{\theta_{0z}}{\rho_0}, \quad (4e)$$

and the linear lower boundary condition writes

$$w'(z=0) = \frac{\bar{u}_g}{a \cos \phi} \frac{\partial h}{\partial \lambda}. \quad (5)$$

In (4)-(5), the prime variables are for the disturbance fields produced by the mountain, $\rho_0(z)$ is a background density profile, $\rho_r = \rho_0(0)$, u_g and v_g are the two components of the geostrophic wind,

$$u_g = -\frac{1}{af} \frac{\partial \Phi}{\partial \phi}, \quad v_g = \frac{1}{af \cos \phi} \frac{\partial \Phi}{\partial \lambda}, \quad (6)$$

u , v , and w are the three components of the wind, and θ is the potential Temperature.

Two unconventional terms are introduced in (4b) and (4e). The first is the lateral force $F' \delta(z) / \rho_r$, where $\delta(z)$ is the Dirac distribution. It will only be used in a formal way, in order to clarify the relation between the mountain forces applied to the atmosphere and the more conventional boundary condition in (5). In (4e) the diabatic term $Q'(\lambda, \phi) \theta_{0z} / \rho_0$ will be used to represent more realistically the interaction between the low-level wind and the mountain (see section 3).

b. Model description

To analyze the response in our model, we will first follow Bretherton (1966), and assume that (4a)-(4e), which are written for $z \geq 0$, are valid for all z once multiplied by the Heaviside function $\mathcal{H}(z)$. Hence, if we derive a PV budget from 4a-4e, we obtain the PV equation:

$$\left[\left(\frac{\partial}{\partial t} + \frac{\bar{u}_g}{a \cos \phi} \frac{\partial}{\partial \lambda} \right) q'_g + \frac{v'_g}{a} \bar{q}_{g\phi} \right] \mathcal{H}(z) \quad (7a)$$

$$+ \left[\left(\frac{\partial}{\partial t} + \frac{\bar{u}_g}{a \cos \phi} \frac{\partial}{\partial \lambda} \right) f \frac{\Phi'_z}{N^2} - \frac{f^2 \bar{u}_{gz}}{N^2} v'_g + f w' - \frac{F'_\lambda}{\rho_r a \cos \phi} - \frac{f Q'}{2\theta_{0z}} \right] \delta(z) = 0. \quad (7b)$$

where we have used that $\delta(z) = \mathcal{H}_z(z)$. In (7a) the inflow QG-PV is given by:

$$q_g = \frac{v_{g\lambda} - (u_g \cos \phi)_\phi}{a \cos \phi} + \frac{f}{\rho_0} \left(\frac{\rho_0 \Phi_z}{N^2} \right)_z. \quad (8)$$

To represent a high surface pressure anomaly poleward of (λ_r, ϕ_r) we impose a negative background low level wind $\bar{u}_g(\phi_r, z = 0) < 0$. To represent the subtropic to pole negative temperature gradient, we will consider that the background wind has a positive vertical wind shear characterized by the constant $\Lambda > 0$:

$$\bar{u}_g(\phi, z) = (u_r + \Lambda z) \cos \phi \quad (9)$$

where $u_r < 0$ is a constant and where the $\cos \phi$ dependence is introduced because it simplifies considerably the lower boundary condition (7b). The zonal wind in (9) has a mean QG-PV

$$\bar{q}_g = -\frac{(\bar{u}_g \cos \phi)_\phi}{a \cos \phi} + \frac{f(\rho_0 \bar{\Phi}_z)_z}{N^2 \rho_0} = \left(2 \frac{u_r + \Lambda z}{a} + \frac{a f^2 \Lambda}{N^2 H} \right) \sin \phi. \quad (10)$$

which varies in the meridional direction. Nevertheless, its meridional gradient $\bar{q}_{g\phi}/a$ compares in amplitude with the planetary PV gradient. As the planetary PV gradient is not taken into account in the f -plane approximation we make, we will consistently neglect the influence of $\bar{q}_{g\phi}$ on the evolution of the disturbances.

With this approximation, the disturbance inflow PV q'_g stays null if it is null at $t = 0$ (see Eq. 7a), yielding to

$$\Delta\Phi' + \frac{f^2}{\rho_0} \left(\frac{\rho_0\Phi'_z}{N^2} \right)_z = 0 \quad (11)$$

where $\Delta = \frac{1}{a^2 \cos \phi} \frac{\partial}{\partial \phi} \cos \phi \frac{\partial}{\partial \phi} + \frac{1}{a^2 \cos^2 \phi} \frac{\partial^2}{\partial \lambda^2}$. Using the kinematic boundary condition (5), the lower boundary condition (7b) becomes,

$$\left(\partial_t + \frac{u_r}{a} \partial_\lambda \right) \Phi'_z - \frac{\Lambda}{a} \frac{\partial \Phi'}{\partial \lambda} = -\frac{N^2 u_r}{a} \frac{\partial h}{\partial \lambda}, \quad (12)$$

where we have set the unconventional terms $F' = Q' = 0$. The solutions to (11)-(12) can be computed using the spherical harmonic functions $Y_l^m(\lambda, \phi)$, where $\Delta Y_l^m = -\frac{l(l+1)}{a^2} Y_l^m$ and $\partial_\lambda Y_l^m = im Y_l^m$. In this formalism, we can project Φ' and h on the Y_l^m 's: Φ' writes

$$\Phi'(\lambda, \phi, z, t) = \sum_{l=1}^L \sum_{m=-l}^{+l} \Phi_l^m(t) e^{-k_l z} Y_l^m(\lambda, \phi) \quad (13a)$$

$$h(\lambda, \phi) = \sum_{l=1}^L \sum_{m=-l}^{+l} h_l^m(t) Y_l^m(\lambda, \phi) \quad (13b)$$

where L is the truncation, and where

$$k_l = \left(\frac{1}{4H^2} + \frac{N^2 l(l+1)}{f^2 a^2} \right)^{\frac{1}{2}} - \frac{1}{2H} > 0. \quad (14)$$

The exponential term in (13a) ensures that the disturbance has 0-PV and vanishes in $z = \infty$.

If we take as initial condition that the flow at $t = 0$ is undisturbed ($\Phi_l^m = 0$ at $t = 0$) then a solution that satisfies the linear boundary condition in (12) is:

$$\Phi_l^m(t) = \frac{1 - \exp\left(-\frac{imu_r}{ak_l} \left(k_l + \frac{\Lambda}{u_r}\right) t\right)}{k_l + \frac{\Lambda}{u_r}} N^2 h_l^m. \quad (15)$$

c. Equatorial Mountain Torques in the model

We can calculate two different contributions to the equatorial torques from our model.

The first is the one associated with the background surface pressure gradient,

$$f\bar{u}_g(0) = -\frac{1}{a} \frac{\partial \bar{\Phi}_s}{\partial \phi} = -\frac{1}{\rho_r} \frac{1}{a} \frac{\partial \bar{P}_s}{\partial \phi}, \quad (16)$$

and that is present at the initial time in our model. If we take \bar{P}_s for the pressure in the Equatorial torques in (1a) and (1b) we obtain at $t = 0$:

$$\hat{T}_{X1} = -a^3 f \rho_r \iint \sin \lambda \cos \phi \bar{u}_g(\phi) h(\lambda, \phi) d\lambda d\phi \approx -a f \rho_r \bar{u}_g(\phi_r) V > 0(NH) \quad (17a)$$

$$\hat{T}_{X2} = a^3 f \rho_r \iint \cos \lambda \cos \phi \bar{u}_g(\phi) h(\lambda, \phi) d\lambda d\phi \approx 0, \quad (17b)$$

where the hat symbol is to indicate that these torques are issued from the model. For each mountain, they are expressed in the rotated axis system used to define the regional torques in section 2. The approximate values to the right of (17a)-(17b), where V is the mountain volume, are given to indicate that at $t = 0$ the EMT is essentially along the first rotated equatorial axis, simply because $\sin \lambda \approx 1$ and $\cos \lambda \approx 0$ where the mountain is located and according to the rotated axes. The sign for \hat{T}_{X1} is related to the fact that $u_r < 0$ and to the sign of the Coriolis parameter so it is positive in the Northern Hemisphere and negative in the Southern Hemisphere.

In this paper we argue that those torques measure the dynamical forcing of the mountain on the flow. This assumption is not so obvious at this stage, since the evaluation of the torque in (1) is just a diagnostic where a given surface pressure field is placed in given integrals. To illustrate how this torque impacts the future evolution of the flow, it is worth noting that

the model equations (7a)-(7b) remain unchanged if we impose

$$w'(z = 0) = 0, \quad F' = -\rho_r f \bar{u}_g(\phi, z = 0)h, \quad (18)$$

rather than $F' = 0$ and w' given by (5), as was done before. Note also that the stress F' in (18) corresponds to the lift force associated with vortex compression by mountains in Smith (1979), which was introduced in a GCM by Lott (1999) to reduce its systematic errors.

To translate this stress F' into a torque, we form the cross product between the position vector \mathbf{r} and the momentum Eqs. (4a)–(4b) and integrate over all the atmosphere. When doing so, the EMT vector due to the surface stress F' is:

$$\mathbf{T}_F = a^3 \int \int_{\lambda, \phi} F'(\cos\phi \sin\lambda, -\cos\phi \cos\lambda) d\phi d\lambda. \quad (19)$$

If we use F' from (18), the torque in (19) is exactly equal to the initial torque in (1), providing that $\partial \bar{P}_S / \partial \phi = -af\rho_r \bar{u}_g(\phi, z = 0)$. As F' is now (i) the only forcing in the model, (ii) purely dynamical, and (iii) builds up a global torque exactly equal to the equatorial mountain torques, it is now justified to say that the equatorial mountain torque measures the dynamical forcing of the flow by the mountain.

The mountain torque predicted by the model and using the torque expressions (1a)-(1b) evolves simply because the surface pressure field $\rho_r \Phi(z = 0)$ is not constant. Nevertheless, the evolution of the torque in this case is purely diagnostic because the disturbance signal does not interact in return with the orography (the model is linear). It means that this model can explain how an initial torque along the first axis \hat{T}_{X1} produces a torque along the second axis \hat{T}_{X2} at a later stage, but it can not tell how this second torque can affect \hat{T}_{X1} in return. Hence, we will always present $\hat{T}_{X1}(t = 0)$ resulting from the background flow only,

and $\hat{T}_{X2}(t = 1 \text{ day})$. Note that $\hat{T}_{X2}(t = 1 \text{ day})$ is essentially due to the disturbance field since the contribution of the background flow to it is small (see (17b)).

4. Model results and comparison with the composites

a. Experimental setup

With the model described above, we analyzed the cases of the Tibetan Plateau, the Rockies, and the Andes. In latitude, we will center our model at a latitude ϕ_r that is in between the midlatitudes and the subtropics, with $\phi_r = +30^\circ\text{N}$ for the TP and the Rockies and $\phi_r = -30^\circ\text{S}$ for the Andes. We will also assume that the atmosphere at rest is isothermal ($T_0(z) = T_r = 285 \text{ K}$), which results in a mean density $\rho_0(z) = \rho_r \exp(-z/H)$ where $H = RT_r/g = 8340 \text{ m}$ and $\rho_r = 1.24 \text{ kg m}^{-3}$, and a mean potential temperature $\theta_0(z) = T_r e^{2z/7H}$. From these parameters, it follows that the Brünt Väisälä frequency $N = 1.83 \cdot 10^{-2} \text{ s}^{-1}$. This value is quite large compared to standard tropospheric values, but we have found that in our composites the characteristic values for N are around $N = 1.5 \cdot 10^{-2} \text{ s}^{-1}$ between the surface and 500 hPa (not shown). This value is not too far from the isothermal value considered in the model.

To define the topography, we use the NCEP/NCAR topography filtered at the truncation T21 and multiplied by a smooth plateau function (see details in the caption of Fig. 8). This smoothing is consistent with the fact that the composite patterns in Figs. 5-6-7 are dominated by large horizontal scales, with wavelengths around or larger than 20° in longitude or latitude. To be consistent, we also verified that the EMT series are not much affected by this filtering

(see Table (3)).

The background flow parameters u_r and Λ in (9), are adjusted to the prevailing wind conditions found in the composites along the eastern flank of the massif analyzed. The values of the wind are taken from the eastern flanks because the cold surges develop there. Note that the composites for the zonal wind used for this purpose include the annual cycle.

b. Evolution of the surface fields and equatorial torques

For the TP, the low level wind constant in (9) has been set to $u_r = -4 \text{ m s}^{-1}$, which gives a low-level background wind at 30°N $\bar{u}_g(\phi_r, z = 0) = -3.46 \text{ m s}^{-1}$. This value is coherent with the composite low-level zonal wind velocities at 30°N along the Eastern flank of the TP shown in Fig. 9. Still according to Fig. 9, we take for the shear parameter $\Lambda = 5.2 \cdot 10^{-3} \text{ s}^{-1}$, so the background zonal wind in the model is around 58 m s^{-1} at 200 hPa and 30°N . Note also that with the orography in Fig. 8b, the low level wind value $u_r = -4 \text{ m s}^{-1}$ yields to a an equatorial mountain torque $\hat{T}_{TP1} = 63 \text{ Ha}$ in the theoretical model (17a), that compares with the peak composite value of \tilde{T}_{TP1} in Fig. 4a (72 Ha). A similar tuning of the flow parameters using the composites for the Rockies and the Andes in Figs. 9bc leads to $u_r = -5 \text{ m s}^{-1}$ for both and $\Lambda = 3.3 \cdot 10^{-3} \text{ s}^{-1}$ for the Rockies and $\Lambda = 3.1 \cdot 10^{-3} \text{ s}^{-1}$ for the Andes. From these setups it follows that $\hat{T}_{R1} = 29 \text{ Ha}$ and $\hat{T}_{Ad1} = -12 \text{ Ha}$, again values that compare reasonably well with those in the composites at D0 and which are around 37 Ha and -16 Ha respectively (Table (4))

Figure 10 shows the disturbance surface pressure and surface temperature in the theoretical model after 1 day of integration for the TP. The choice of this 1-day interval here and

for the other mountains is motivated by the fact that in the composites, the anomalies on the eastern flanks of the mountains develop on such a time scale (Figs. 4a-c). On the eastern flank of the TP, the model predicts a rise in surface pressure of about 7 hPa and a drop in surface temperature of about 7 K (Fig. 10) both centered around (105 – 110°E, 30 – 35°N) and that are reminiscent of the structure obtained in the composite at lag D+2 in Figs. 5ef. However, to the west of the longitude $\lambda = 95^\circ\text{E}$, the linear model predicts a drop in surface pressure and a rise in surface temperature which are absent from the composites.

For the Rockies and the Andes the results from the model have the same level of realism when compared to their corresponding composites (not shown): the model predicts a realistic large scale pressure increase and a large scale temperature decrease to the east of the mountains, as well as changes of the opposite sign to the west of the mountains.

From the surface pressure pattern in Fig. 10, and coming back for instance to the schematic picture in Fig. 1, it is clear that the interaction between the TP and the flow at that time yields to a negative torque along the second equatorial axis. If we evaluate it from the model by using (1b) we find that $\hat{T}_{TP2}(t = 1 \text{ day}) = -32 \text{ Ha}$, and is largely superior in amplitude when compared to the fastest change in \tilde{T}_{TP2} that occurs in one day in the composite ($\Delta\tilde{T}_{TP2} = \tilde{T}_{TP2}(D + 1) - \tilde{T}_{TP2}(D0) = -12 \text{ Ha}$ in Fig. 4). For the Andes and the Rockies, the discrepancy is not as pronounced (see Table 4), providing that we take into account that in these two regions the cold surges have started to develop around D-1. This is clearly apparent for the composite of surface Temperature at D0 in Figs. 6d and 7d. As a result, and for these two massifs, the largest 1-day change in \tilde{T}_{2X} is between D-1 and D0 (see Fig. 4). For the Rockies the model predicts a torque $\hat{T}_{R2} = -19.8 \text{ Ha}$ that corresponds to $\Delta\tilde{T}_{R2} = \tilde{T}_{R2}(D0) - \tilde{T}_{R2}(D - 1) = -19.7 \text{ Ha}$. For the Andes, as for the TP, the torque is

overestimated: $\hat{T}_{Ad2} = 11.6$ Ha whereas $\Delta\tilde{T}_{Ad2} = \tilde{T}_{Ad2}(D0) - \tilde{T}_{Ad2}(D - 1) = 8.7$ Ha.

c. Results with a modified lower boundary condition

The unrealistic surface responses that occur in the model to the west of the massifs considered are due to the linear boundary condition in (12), to the positive mountain slope $\partial_\lambda h$ west of the mountain crests, and to the zonally uniform low level wind $\bar{u}_g(z = 0)$. In reality however, the region west of the crests of the mountains corresponds either to very high altitudes, where the surface wind is essentially positive according to the zonal wind composite in Fig. 9, or to more moderate altitudes where the zonal wind composite is almost null near the ground (see again Fig. 9). These effects can be accounted for by using the lower boundary condition in (7b), with $w' = 0$ and F' as in (18), but taking Q' such that (7b) becomes

$$\left(\partial_t + \frac{u_r}{a}\partial_\lambda\right)\Phi'_z - \frac{\Lambda}{a}\frac{\partial\Phi'}{\partial\lambda} = -\frac{N^2 u_r}{a} \text{Min}\left(\frac{\partial h}{\partial\lambda}, 0\right). \quad (20)$$

This correction annihilates the forcing when the slopes are positive, but does not modify the torque $\hat{T}_{X1}(t = 0)$ since F' is not changed and since Q' does not enter into the momentum equation. This term counteracts the fact that the linear boundary condition (12) is unrealistic over the western slopes of the mountains (Fig. 10). From now on, the boundary condition (20) will be called *modified boundary condition*.

For the TP, the surface patterns obtained in this case (Fig. 11ab) are much closer to the composites, essentially because the model response is now almost null to the west of 95°E . To make the comparison between the model at day 1 and the evolution in the composites even more precise, Fig. 11cd shows the difference in the composite fields between D+1 and

D0. This comparison shows that the rise in surface pressure of about 10 hPa and the drop in surface temperature of about 6 K predicted by the model (Fig. 11ab) corresponds quite well to the variations during the first day in the composite, which are around 9 hPa and 7 K respectively (Fig. 11cd). Note that in the composite, the maximum in surface pressure and the minimum in surface temperature are slightly to the west and to the south of the ones predicted by the model. However, the extension of the surface temperature signal as predicted by the model corresponds quite well with the composite.

Another interesting property of the model is that it predicts a dome of cold air trapped in the lower half of the troposphere over the eastern slopes of the mountains (Fig. 12a). This vertical structure is also found in the zonal vertical section from the composite in Fig. 12b. In this sense the model reproduces the well-known vertical structure of the temperature signals associated to the cold surges (e.g. Garreaud 2001, and refs. therein).

For the Rockies, Fig. 13 shows that the model has some skill in reproducing the initial development of the cold surges as observed in the composites. It predicts a temperature drop of 6 K (Fig. 13b) that only slightly exceeds the largest 1-day tendency from the composites in Fig. 13d. The prediction of the location of the temperature signal is also quite good, and the model predicts a rise of 8 hPa in the surface pressure (Fig. 13a), which compares with the value observed in the composite (9 hPa, see Fig. 13c). Accordingly, the signal on the second EMT component ($\hat{T}_{R2}(t = 1 \text{ day}) = -14.9 \text{ Ha}$) compares well with the largest 1-day \tilde{T}_{R2} tendency in the composite ($\Delta\tilde{T}_{R2} = -19.7 \text{ Ha}$, see also Fig. 4b and Table (4)).

For the Andes, the model predicts a 1-day temperature drop up to 5 K in one day east of the Andes (Fig. 14b), which is also the value given by the composite in Fig. 14d, the location of this temperature anomaly being well reproduced. For the surface pressure, the

model (Fig. 14a) only captures a part of the signal observed in the corresponding composite (Fig. 14c), namely the part of the signal which is confined to the eastern flank of the mountains. There, the surface pressure increase in the model is near 10 hPa (Fig. 14a), whereas it is 8 hPa in the composite (Fig. 14c). These last correspondences explain that the second EMT signal from the model ($\hat{T}_{Ad2}(1d) = 7.3 \text{ Ha}$) compares well with the largest 1-day tendency in the composites ($\Delta\tilde{T}_{Ad2} = 8.7 \text{ Ha}$, see also Fig. 4c and Table (4)). The vertical structure of the cold dome from the model (not shown) is also similar to Fig. 7 from Garreaud (2000), which shows the meridional and vertical extension of the cold domes associated to the south-american cold surges.

5. Summary and discussion

The two components of the EMT associated with three major mountain massifs (the TP, the Rockies and the Andes) have been analyzed in the NCEP reanalysis data. When the first equatorial axis is placed at 90 degrees to the west of the massif and the second equatorial axis at the longitude of the center of mass of the massif, the strong signals on \tilde{T}_{X1} are followed one or two days later by strong signals of the opposite sign on \tilde{T}_{X2} (Figs. 3 and 4). These regional contributions partly explain why the two equatorial components of the global mountain torque rotate westward in the equatorial plane (Fig. 2). Their contributions can add up constructively to the contribution of Antarctica, which is the major single contributor to the global equatorial torque, and whose equatorial torque also rotates westward (Fig. 3d).

Returning to the TP and the Rockies, the composites of the surface pressure fields in Figs. 5 and 6 respectively show that a positive signal in \tilde{T}_{X1} is in general associated with

anomalies in surface pressure located poleward of the massif considered. As time evolves, these anomalies shift along the eastern flank of the massif considered which explains the negative signal on \tilde{T}_{X2} . This characteristic evolution of the surface pressure also occurs around the Andes (Fig. 7), provided the sign of the equatorial torques is inverted (due to the fact that the Andes are located in the southern hemisphere). Interestingly the evolution of the surface temperature and surface pressure east of these three massifs is very pronounced, and strongly reminiscent of what occurs during the cold surges that severely affect the weather to their eastern side.

From these observational results, we make two hypotheses: (i) the equatorial mountain torques measure the dynamical forcing of the cold surges by the mountains, and (ii) this dynamical forcing is a substantial driver of the cold surges.

To support these two hypotheses, we develop a mechanistic model for the cold surges that only contains the basic ingredients needed to explain the above observations. For this purpose, we follow Smith (1984) and adapt the quasi-geostrophic *f-plane* Eady (1949) model for baroclinic flow by introducing a mountain forcing via a free-slip lower boundary condition, and by formulating this model on a sphere. It is then shown that, in this framework, the free-slip boundary condition is locally strictly equivalent to a lateral force (that is a force which is perpendicular to the surface wind), and that the amplitude of this lateral force, given in (18), is consistent with the mountain “lift” forces given in Smith (1979). When the low-level background flow is easterly, this lift force results in a positive mountain torque \hat{T}_{X1} (in the northern hemisphere) which is comparable to the one observed.

If we impose that at $t = 0$ the disturbance field is null in this model, high pressure and low temperature anomalies develop in one day along the eastern flank of the massif.

When the low level wind and the upper level shear correspond to the values observed at D0 in the composites keyed on the peaks in \tilde{T}_{X1} , the 1-day tendencies of the model responses in pressure and temperature are compatible to the ones observed in the composites of the reanalysis data immediately after the peaks in \tilde{T}_{X1} . Note that from the surface pressure anomalies predicted by this mechanistic model we can evaluate a tendency on the torque along the second axis \hat{T}_{X2} , which is also comparable in amplitude with the one observed. As many other theoretical models for orographic flows (e.g. that of Smith (1984) for instance) our model simplifies considerably the basic setup and initial conditions. It is used here mainly to show that mountain forces translating in EMTs that are about the amplitude found in reality are strong enough to initiate cold surges in less than few days. A more realistic treatment of the synoptic systems that yields to the peaks in \tilde{T}_{X1} (i.e. the initial condition in the model) would certainly improve our dynamical understanding of the life-cycle of the cold surges.

As our results suggest that the existence of poleward forces imposed by the mountain yields to cold surges in a linear baroclinic context, it needs to be put in perspective with the other explanations for the cold surges that have been proposed in the past. In many aspects they actually complement them. Some theories attribute the clockwise displacement of cold surges to topographic Rossby or Kelvin waves (e.g. Hsu 1987; Compo et al. 1999, and refs. therein). Other theories attribute the equatorward propagation of the cold surges to nonlinear processes, where the cold advection by the meridional wind is the main contributor. This interpretation is in good part supported by model and diagnostic studies (e.g. Sumi 1983; Colle and Mass 1995; Garreaud 2000). All these theories for the cold surge propagation request the presence of a preexisting inversion near or below the mountain top, and do not

take into account the background flow.

However, Reason (1994) has suggested that linear mechanisms and the effect of the background flow are important to provide a large scale preconditioning of the cold surges at least over the Andes and TP. Our model, by taking into account the interaction of the large scale background flow with the orography, follows this line of work. It explains how the mountain forcing can trigger the initial development of a cold surge by building up rapidly the dome of cold air in which low level orographically trapped sub-synoptic disturbances can subsequently develop (Fig. 12a).

In the past studies about the equatorial AAM budget, it has been shown that the evolution of the EAAM is largely dominated by the equivalent barotropic planetary waves with zonal wavenumber $s = 1$, and that the mountain torque has a rather small impact on these waves (Egger and Hoinka (2002)). On the contrary the evolution of the mass term plays an important role in the EAAM evolution associated with planetary barotropic waves. In the present study, the focus is on much smaller spatial scales so we do not try to address this problem. The model used is in fact not adapted to this purpose since it is based on the anelastic approximation which filters out the equivalent barotropic waves, and which has an AAM budget that does not contain mass terms (not shown). Another reason for not trying to address the response of the EAAM to the Equatorial Torques is that the EAAM budget is not well closed in the reanalysis data. It is thus extremely difficult to establish where the EAAM anomalies produced by regional EMTs are in fact redistributed. Our model results are only indicative in this respect, the high surface pressure patterns eastward of the mountains (and produced by a positive \tilde{T}_{M1}) corresponding to large scale anticyclones which can affect the two components of the Equatorial AAM.

From a practical viewpoint, these results concerning the significance of mountain-induced lateral (or lift) forces for the regional weather can be helpful to tell if a GCM represents well the mountains. To do so, our results indicate that one should diagnose the equatorial components of the mountain torque and not only its axial component (as it is done in Brown (2004) or in Lott et al. (2005)).

In GCMs, there are essentially two ways to modify these lift forces. One is very efficient, and consists in modifying the elevation of the explicit model orography (yielding for instance to the envelope orography in Wallace et al. (1983)). However, this solution is not completely satisfactory since it increases the number of places that are below the ground in models. An alternative solution consists in parameterizing them as it was done here with our term F' in (18) but distributing it over a finite depth. This depth could be the depth of the valleys in which we consider that the large-scale flow does not enter, to follow the arguments in Wallace et al. (1983) (see also Eq. (5) in Lott (1999)). The fact that this term F' can be significant for the synoptic weather in key regions of the climate system stresses its potential significance for coupled climate models. To illustrate this importance, the study of Kitoh (2004) is very instructive. It shows that in a state of the art coupled model, the simulation of monsoon precipitations is very sensitive to the large-scale mountain elevation. To support that these issues may well be important for the monsoon predictions, it is also important to recall here that Mailler and Lott (2009) found that the signals on the Equatorial mountain torques due to the TP are followed by increased winter monsoon precipitation.

acknowledgments

The NCEP Reanalysis data was kindly provided by the NOAA/OAR/ESRL PSD, Boulder, Colorado, USA, from their Web site at <http://www.cdc.noaa.gov/>.

REFERENCES

- Bessemoulin, P., P. Bougeault, A. Genoves, A. J. Clar, and D. Puech, 1993: Mountain pressure drag during PYREX. *Beitr. Phys. Atmosph.*, **66**, 305–325.
- Bretherton, F. P., 1966: Critical layer instability in baroclinic flows. *Q. J. R. Meteorol. Soc.*, **92**, 325–334.
- Brown, A. R., 2004: Resolution dependence of orographic torques. *Q. J. R. Meteorol. Soc.*, **130**, 3029–3046.
- Buzzi, A. and S. Tibaldi, 1978: Cyclogenesis in the lee of the alps: a case study. *Q. J. R. Meteorol. Soc.*, **104**, 271–287.
- Chang, C.-P., J. E. Erickson, and K. M. Lau, 1979: Northeasterly cold surges and near-equatorial disturbances over the winter MONEX area during december 1974. part i: Synoptic aspects. *Mon. Weather Rev.*, **107**, 812–829.
- Chang, C.-P. and K. M. Lau, 1980: Northeasterly cold surges and near-equatorial disturbances over the winter MONEX area during december 1974. part ii: Planetary-scale aspects. *Mon. Weather Rev.*, **107**, 812–829.
- Chen, T.-C., W.-R. Huang, and J.-H. Yoon, 2004: Interannual variation of the east-asian cold surge activity. *J. Clim.*, **17**, 401–413.

- Clark, J. H. E., 1990: An observational and theoretical study of Colorado lee cyclogenesis. *J. Atmos. Sci.*, **47**, 1541–1561.
- Colle, B. A. and C. Mass, 1995: The structure evolution of cold surges east of the Rocky Mountains. *Mon. Weather Rev.*, **123**, 2577–2610.
- Compo, G. P., G. N. Kiladis, and P. J. Webster, 1999: The horizontal and vertical structure of east asian winter monsoon pressure surges. *Q. J. R. Meteorol. Soc.*, **125**, 29–54.
- Davies, H. C. and P. D. Phillips, 1985: Mountain drag along the Gotthard section during ALPEX. *J. Atmos. Sci.*, **42**, 2093–2109.
- Eady, E. T., 1949: Long waves and cyclone waves. *Tellus*, **1**, 33–52.
- Egger, J., 1988: Alpine lee cyclogenesis: Verification of theories. *J. Atmos. Sci.*, **45**, 2187–2203.
- Egger, J. and K.-P. Hoinka, 2000: Mountain torques and the equatorial components of global angular momentum. *J. Atmos. Sci.*, **57**, 2319–2331.
- Egger, J. and K.-P. Hoinka, 2002: Equatorial components of global atmospheric angular momentum: Covariance functions. *Q. J. R. Meteorol. Soc.*, **128**, 1137–1157.
- Egger, J. and K.-P. Hoinka, 2008: Mountain torque events at the Tibetan Plateau. *Mon. Weather Rev.*, **136**, 389–404, doi:10.1175/2007MWR2126.1.
- Egger, J., K. Weickmann, and K.-P. Hoinka, 2007: Angular momentum in the global atmospheric circulation. *Rev. Geophys.*, **45**, RG4007, doi:10.1029/2006RG000213.

- Feldstein, S. B., 2006: Dynamical processes of equatorial atmospheric angular momentum. *J. Atmos. Sci.*, **63**, 565–581, doi:10.1175/JAS3586.1.
- Garreaud, R. D., 2000: Cold air incursions over subtropical South America: Mean structure and dynamics. *Mon. Weather Rev.*, **128**, 2544–2559.
- Garreaud, R. D., 2001: Subtropical cold surges: regional aspects and global distribution. *Int. J. Climatol.*, **21**, 1181–1197.
- Hsu, H.-H., 1987: Propagation of low-level circulation features in the vicinity of mountain ranges. *Mon. Weather Rev.*, **115**, 1864–1892.
- Hsu, H.-H. and J. M. Wallace, 1985: Vertical structure of wintertime teleconnection patterns. *J. Atmos. Sci.*, **42**, 1693–1710.
- Iskenderian, H. and D. A. Salstein, 1998: Regional sources of mountain torque variability and high-frequency fluctuations in atmospheric angular momentum. *Mon. Weather Rev.*, **126**, 1681–1694.
- Kalnay, E., et al., 1996: The NCEP/NCAR 40-year reanalysis project. *Bull. Am. Meteorol. Soc.*, **77**, 437–471.
- Kitoh, A., 2004: Effects of mountain uplift on east asian summer climate investigated by a coupled atmosphere-ocean GCM. *J. Clim.*, **17**, 783–802.
- Lott, F., 1999: Alleviation of stationary biases through a mountain drag parameterization scheme and a simple representation of mountain lift forces. *Mon. Weather Rev.*, **127**, 788–801.

- Lott, F. and F. d'Andrea, 2005: Mass and wind axial angular momentum responses to mountain torques in the 1-25 day band. links with the arctic oscillation. *Q. J. R. Meteorol. Soc.*, **131**, 1483–1500, doi:10.1256/qg.03.168.
- Lott, F., L. Goudard, and A. Martin, 2005: Links between the mountain torque and the Arctic Oscillation in the Laboratoire de Météorologie dynamique (LMDz), general circulation model. *J. Geophys. Res.*, **110**, D22 107, doi:10.1029/2005JD006073.
- Lott, F., A. W. Robertson, and M. Ghil, 2004: Mountain torques and northern hemisphere low-frequency variability. Part I: Hemispheric aspects. *J. Atmos. Sci.*, **61**, 1259–1271.
- Mailler, S. and F. Lott, 2009: Dynamical influence of the Tibetan Plateau on winter monsoon convection over southeast Asia. *Geophys. Res. Lett.*, **36**, L06708, doi:10.1029/2008GL036952.
- Marengo, J., A. Cornejo, P. Satyamurty, and C. Nobre, 1997: Cold surges in tropical and extratropical South America: The strong event in june 1994. *Mon. Weather Rev.*, **125**, 2759–2786.
- Pierrehumbert, R. T., 1985: A theoretical model of orographically modified cyclogenesis. *J. Atmos. Sci.*, **42**, 1244–1258.
- Reason, C. J. C., 1994: Orographically trapped disturbances in the lower atmosphere: scale analysis and simple models. *Meteorol. Atmos. Phys.*, **53**, 131–136.
- Rosen, R. D. and D. A. Salstein, 1983: Variations in atmospheric angular momentum on global and regional scales and the length of day. *J. Geophys. Res.*, **88**, 5451–5470.

- Schultz, D. M., W. E. Bracken, L. F. Bosart, G. J. Hakim, M. A. Bedrick, M. J. Dickinson, and K. R. Tyle, 1997: The 1993 superstorm cold surge: Frontal structure, gap flow, and tropical impact. *Mon. Weather Rev.*, **125**, 5–39.
- Seluchi, M. E. and J. T. Nery, 1992: Condiciones meteorológicas asociadas a la ocurrencia de heladas en la región de Maringá (in spanish). *Rev. Brasileira Meteor.*, **7**, 523–534.
- Slingo, J. M., 1998: Extratropical forcing of tropical convection in a northern winter simulation with the UGAMP GCM. *Q. J. R. Meteorol. Soc.*, **124**, 27–51.
- Smith, R. B., 1979: Some aspects of the quasi-geostrophic flow over mountains. *J. Atmos. Sci.*, **36**, 2385–2392.
- Smith, R. B., 1984: A theory of lee cyclogenesis. *J. Atmos. Sci.*, **41**, 1159–1168.
- Smith, R. B., 1986: Further development of a theory of lee cyclogenesis. *J. Atmos. Sci.*, **43**, 1582–1602.
- Speranza, A., A. Buzzi, A. Trevisan, and P. Malguzzi, 1985: A theory of deep cyclogenesis in the lee of the Alps. Part I: Modifications of baroclinic instability by localized topography. *J. Atmos. Sci.*, **42**, 1521–1535.
- Sumi, A., 1983: A study on cold surges around the Tibetan Plateau by using numerical models. *J. Meteorol. Soc. Jpn*, **63**, 377–396.
- Tangang, F. T., L. Juneng, E. Salimun, P. N. Vinayachandran, Y. K. Seng, C. J. C. Reason, S. K. Behera, and T. Yasunari, 2008: On the roles of the northeast cold surge, the Borneo Vortex, the Madden-Julian Oscillation, and the Indian Ocean Dipole during the extreme

2006/2007 flood in southern Peninsular Malaysia. *Geophys. Res. Lett.*, **35**, L14S07, doi: 10.1029/2008GL033429.

Wallace, J. M., S. Tibaldi, and A. J. Simmons, 1983: Reduction of systematic forecast errors in the ECMWF model through the introduction of an envelope orography. *Q. J. R. Meteorol. Soc.*, **109**, 683–717.

Weickmann, K. M. and P. D. Sardeshmukh, 1994: The atmospheric angular momentum cycle associated with the Madden-Julian Oscillation. *J. Atmos. Sci.*, **51**, 3194–3208.

Zhang, Y., K. R. Sperber, and J. S. Boyle, 1997: Climatology and interannual variation of the east asian winter monsoon: results from the 1979-95 NCEP/NCAR reanalysis. *Mon. Weather Rev.*, **125**, 2605–2619.

List of Tables

- 1 Sectors over which the integrations in (1a) and (1b) are evaluated to measure the individual contributions of each mountain massif to the global torque, and geographical coordinates of the center of mass for each mountain range. Note that the domain sizes here largely contain the massifs considered. 36
- 2 Standard deviation $\left\langle \tilde{T}_{X1}^2 + \tilde{T}_{X2}^2 \right\rangle^{\frac{1}{2}}$ for the global EMT and for the regional contributions of each of the major mountain ranges, expressed in Hadley (Ha). 37
- 3 Percentage of error between the raw mountain torque series and the mountain torque series evaluated after filtering the orography and the surface pressure at different truncations. For all series the annual cycle has been subtracted. For the regional torques the filtered orography is also tapered by the smooth plateau function described in section 4.a. For a given mountain X , a given equatorial axis i , and a given truncation Tnn , the values shown correspond to square of the error: $(\epsilon_{Xi}^{Tnn})^2 = \langle (\tilde{T}_{Xi} - \tilde{T}_{Xi}^{Tnn})^2 \rangle / \langle \tilde{T}_{Xi}^2 \rangle$. 38
- 4 Parameters u_r and Λ used for the model simulations (see (9)), resulting values of $\hat{T}_{X1}(t = 0)$ compared to $\tilde{T}_{X1}(D0)$, value of $\hat{T}_{X2}(t = 1 \text{ day})$ simulated with the complete boundary condition (column \hat{T}_{X2}), and with the modified boundary condition (20) (column \hat{T}_{X2}^m , compared to $\Delta\tilde{T}_{X2}$ from the composites (Fig. 4a-c) 39

Massif	Longitude range [λ_{X1} ; λ_{X2}]	Latitude range [ϕ_{X1} ; ϕ_{X2}]	Center of mass (λ_X ; ϕ_X)
Andes	[90°W-60°W]	[60°S-15°N]	(16.7°S;70.4°W)
Antarctica	[180°W-180°E]	[90°S-60°S]	(83.1°S;79.7°E)
Greenland	[70°W-10°W]	[55°N-85°N]	(72.0°N;43.6°W)
TP	[60°E-120°E]	[15°N-60°N]	(37.8°N;91.5°E)
Rockies	[170°W-90°W]	[15°N-80°N]	(44.9°N;111.3°W)

TABLE 1. Sectors over which the integrations in (1a) and (1b) are evaluated to measure the individual contributions of each mountain massif to the global torque, and geographical coordinates of the center of mass for each mountain range. Note that the domain sizes here largely contain the massifs considered.

Massif	All-year	Winter (DJF)	Summer (JJA)
Global	63.6	60.3	65.2
Antarctica	50.2	36.5	58.1
TP	21.8	26.8	14.9
Greenland	16.8	21.1	11.2
Rockies	15.4	19.1	10.3
Andes	6.0	7.6	4.3

TABLE 2. Standard deviation $\langle \tilde{T}_{X_1}^2 + \tilde{T}_{X_2}^2 \rangle^{\frac{1}{2}}$ for the global EMT and for the regional contributions of each of the major mountain ranges, expressed in Hadley (Ha).

	Global		TP		Antarctica		Rockies		Greenland		Andes	
	T_{M1}	T_{M2}	\tilde{T}_{TP1}	\tilde{T}_{TP2}	\tilde{T}_{At1}	\tilde{T}_{At2}	\tilde{T}_{R1}	\tilde{T}_{R2}	\tilde{T}_{G1}	\tilde{T}_{G2}	\tilde{T}_{Ad1}	\tilde{T}_{Ad2}
T63	< 1%	< 1%	< 1%	< 1%	< 1%	< 1%	< 1%	< 1%	< 1%	< 1%	< 1%	< 1%
T42	< 1%	< 1%	< 1%	< 1%	< 1%	< 1%	< 1%	< 1%	< 1%	< 1%	< 1%	1.9%
T21	3%	3.4%	5.6%	6.1%	2.3%	3.8%	2.1%	4.3%	19%	25%	12%	23%
T10	41%	26%	62%	32%	40%	19.6%	24%	42%	92%	129%	44%	124%

TABLE 3. Percentage of error between the raw mountain torque series and the mountain torque series evaluated after filtering the orography and the surface pressure at different truncations. For all series the annual cycle has been subtracted. For the regional torques the filtered orography is also tapered by the smooth plateau function described in section 4.a. For a given mountain X , a given equatorial axis i , and a given truncation Tnn , the values shown correspond to square of the error: $(\epsilon_{Xi}^{Tnn})^2 = \langle (\tilde{T}_{Xi} - \tilde{T}_{Xi}^{\mathbf{Tnn}})^2 \rangle / \langle \tilde{T}_{Xi}^2 \rangle$.

Massif	u_r (m s ⁻¹)	Λ (10 ⁻³ s ⁻¹)	$\hat{T}_{X1}(t = 0)$ (Ha)	$\tilde{T}_{X1}(D0)$ (Ha)	\hat{T}_{X2} (Ha)	\hat{T}_{X2}^m (Ha)	$\Delta\tilde{T}_{X2}$ (Ha)
Tibet	-4.	5.2	63	72	-32.7	-24.9	-12.2
Rockies	-5.	3.3	29	37	-19.8	-14.9	-19.7
Andes	-5.	3.1	-12	-16	11.6	7.3	8.7

TABLE 4. Parameters u_r and Λ used for the model simulations (see (9)), resulting values of $\hat{T}_{X1}(t = 0)$ compared to $\tilde{T}_{X1}(D0)$, value of $\hat{T}_{X2}(t = 1 \text{ day})$ simulated with the complete boundary condition (column \hat{T}_{X2}), and with the modified boundary condition (20) (column \hat{T}_{X2}^m , compared to $\Delta\tilde{T}_{X2}$ from the composites (Fig. 4a-c)

List of Figures

- 1 Schematic pictures of NH midlatitude and subtropical anomalies in surface pressure yielding to anomalous equatorial torques. This schematic figure is for the Himalayas, and the surface pressure anomalies are representative of two successive stages in the life cycle of an east-asian cold surge. 43
- 2 Spectral analysis of \tilde{T}_{M1} and \tilde{T}_{M2} . (a) coherency between \tilde{T}_{M1} and \tilde{T}_{M2} ; (b) phase difference between \tilde{T}_{M1} and \tilde{T}_{M2} ; (c) spectrum of \tilde{T}_{M1} ; (d) spectrum of \tilde{T}_{M2} . The spectra and the cross-spectrum are deduced from the two periodograms and the cross periodogram of the series, each of them being smoothed by a 80-point 10% cos window. In the frequency domain this yields a resolution of $8 \cdot 10^{-2} \text{cycles/d}$. The mean level (gray solid) and the 99% significance level (gray dashed) are evaluated by a Monte-Carlo procedure, which uses an ensemble of 500 pairs of red noise series whose variances and lag-1 autocorrelations correspond to those of \tilde{T}_{M1} and \tilde{T}_{M2} . 44
- 3 Coherence and phase relationship between (a) $\tilde{T}_{TP,1}$ and $\tilde{T}_{TP,2}$; (b) $\tilde{T}_{R,1}$ and $\tilde{T}_{R,2}$; (c) $\tilde{T}_{Ad,1}$ and $\tilde{T}_{Ad,2}$; and (d) $\tilde{T}_{At,1}$ and $\tilde{T}_{At,2}$. Same conventions and method as in Fig. 2 45
- 4 (a) composite time series of \tilde{T}_{TP1} (gray, solid) \tilde{T}_{TP2} (black, solid) keyed on the 20 strongest positive peaks of \tilde{T}_{TP1} , and corresponding 99% significance levels; (b) same for \tilde{T}_{R1} and \tilde{T}_{R2} keyed on \tilde{T}_{R1} ; and (c) composite time series of \tilde{T}_{Ad1} and \tilde{T}_{Ad2} keyed on the 20 strongest negative peaks of \tilde{T}_{Ad1} 46

- 5 Composite of the surface pressure anomalies (a,c,e,g) and surface temperature anomalies (b,d,f,h) for the 20 strongest positive peaks of \tilde{T}_{TP1} , at lag D-2 (a,b), D0 (c,d), D+2 (e,f) and D+4 (g,h); 99% confidence level (shaded). Contour interval is 2 hPa for the surface pressures, 2 K for the surface temperatures. Zero-contours are omitted. 47
- 6 Same as Fig. 5 but keyed on the positive peaks of \tilde{T}_{R1} 48
- 7 Same as Fig. 5 but keyed on the negative peaks of \tilde{T}_{Ad1} 49
- 8 (a)topography retained for the model run and (b)NCEP topography (meters above sea level). The model topography is obtained by multiplying the T21-filtered NCEP topography by $\alpha(\lambda)\beta(\phi)$, where $\alpha(\lambda)$ (resp. $\beta(\phi)$) is a function whose value is 1 in the interval $[\lambda_1; \lambda_2]$ (resp. $[\phi_1; \phi_2]$) corresponding to the longitude (resp. latitude) range in Table 1; 0 outside $[\lambda_1 - 15^\circ; \lambda_2 + 15^\circ]$ (resp. $[\phi_1 - 15^\circ; \phi_2 + 15^\circ]$); and a smooth connection is ensured by the use of an exponential taper $\varphi(t) = \exp(t^2/(t^2 - 1))$. 50
- 9 (a)composite of the zonal wind at 30°N keyed on the 20 strongest positive peaks of $\tilde{T}_{TP,1}$; (b) same as (a) but for the composite keyed on \tilde{T}_{R1} ; (c) composite of the zonal wind at 30°S keyed on the 20 strongest negative peaks of \tilde{T}_{Ad1} . The contours are every 10 ms^{-1} for positive (westerly) winds, at -3 ms^{-1} and -5 ms^{-1} for negative (easterly) winds. 51

- 10 (a) Sea level pressure tendency between time 0d and time +1d in the model simulation for the Tibetan Plateau (contours every 1 hPa, zero-contour omitted); (b) Surface potential temperature tendency between time 0d and time +1d in the model simulation for the Tibetan Plateau (contours every 1 K, zero-contour omitted) 52
- 11 (a) and (b): same as Fig. 10 but with the modified boundary condition; (c) tendency of \tilde{P}_S between lag 0d and 1d in the composite keyed on the 20 strongest events on \tilde{T}_{TP1} (contours every 1 hPa, zero-contour omitted); (d) tendency of \tilde{T}_{50m} between lag 0d and 1d in the composite keyed on the 20 strongest events on \tilde{T}_{TP1} (contours every 1 K, zero-contour omitted) 53
- 12 (a) air temperature anomaly (K, thin contours) at $32.5^\circ N$ at time +1d in the model simulation. The thick black line represents the model ground elevation. (b) composite of air temperature anomaly (relative to the climatology) 1d after after the 20 strongest peaks in \tilde{T}_{TP1} 54
- 13 Same as Fig. 11 but for the Rockies. The 1d differences in (c) and (d) are between the composites at lag 0d and $-1d$ 55
- 14 Same as Fig. 13 but for the Andes 56

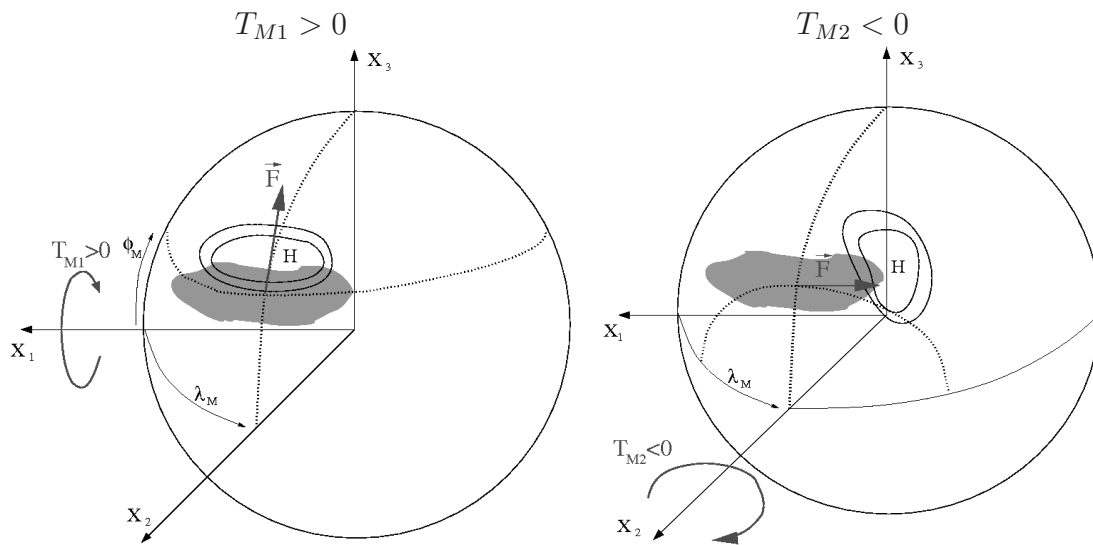


FIG. 1. Schematic pictures of NH midlatitude and subtropical anomalies in surface pressure yielding to anomalous equatorial torques. This schematic figure is for the Himalayas, and the surface pressure anomalies are representative of two successive stages in the life cycle of an east-asian cold surge.

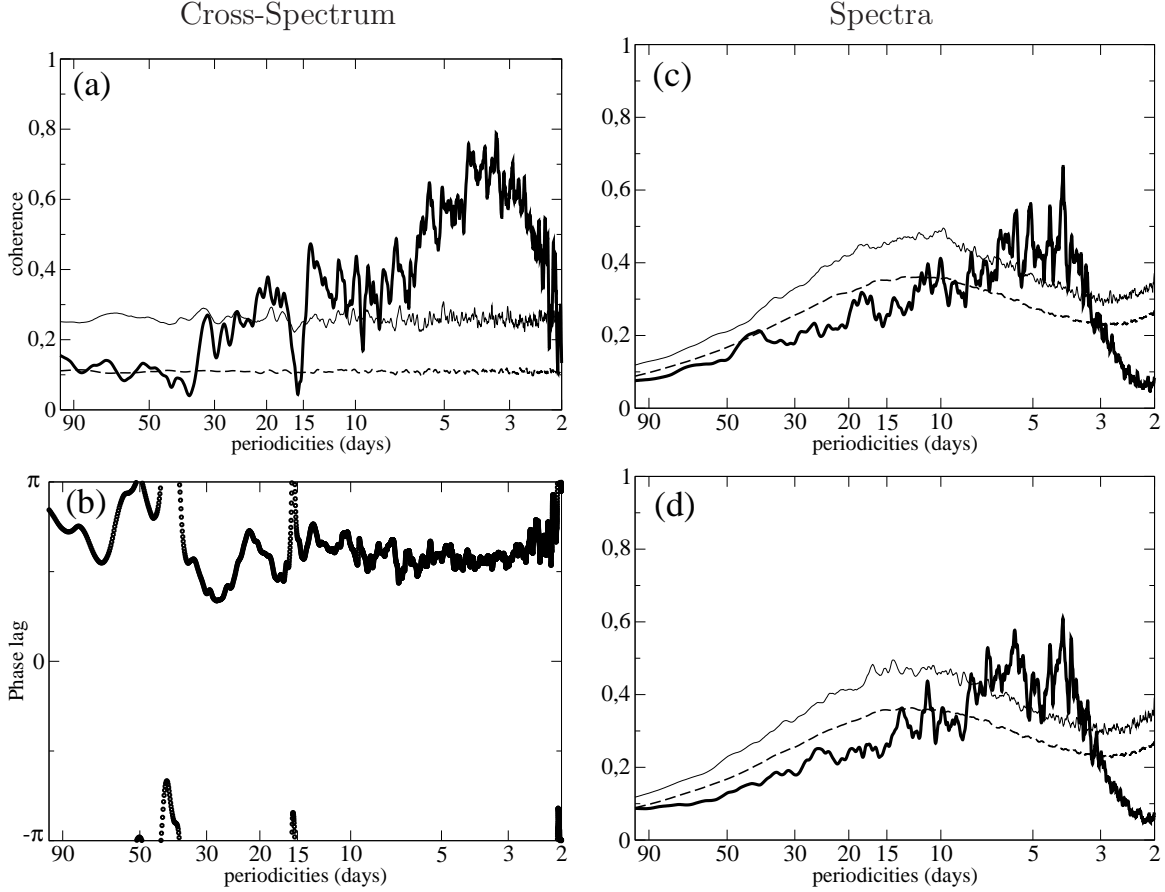


FIG. 2. Spectral analysis of \tilde{T}_{M1} and \tilde{T}_{M2} . (a) coherency between \tilde{T}_{M1} and \tilde{T}_{M2} ; (b) phase difference between \tilde{T}_{M1} and \tilde{T}_{M2} ; (c) spectrum of \tilde{T}_{M1} ; (d) spectrum of \tilde{T}_{M2} . The spectra and the cross-spectrum are deduced from the two periodograms and the cross periodogram of the series, each of them being smoothed by a 80-point 10% cos window. In the frequency domain this yields a resolution of $8 \cdot 10^{-2} \text{cycles/d}$. The mean level (gray solid) and the 99% significance level (gray dashed) are evaluated by a Monte-Carlo procedure, which uses an ensemble of 500 pairs of red noise series whose variances and lag-1 autocorrelations correspond to those of \tilde{T}_{M1} and \tilde{T}_{M2} .

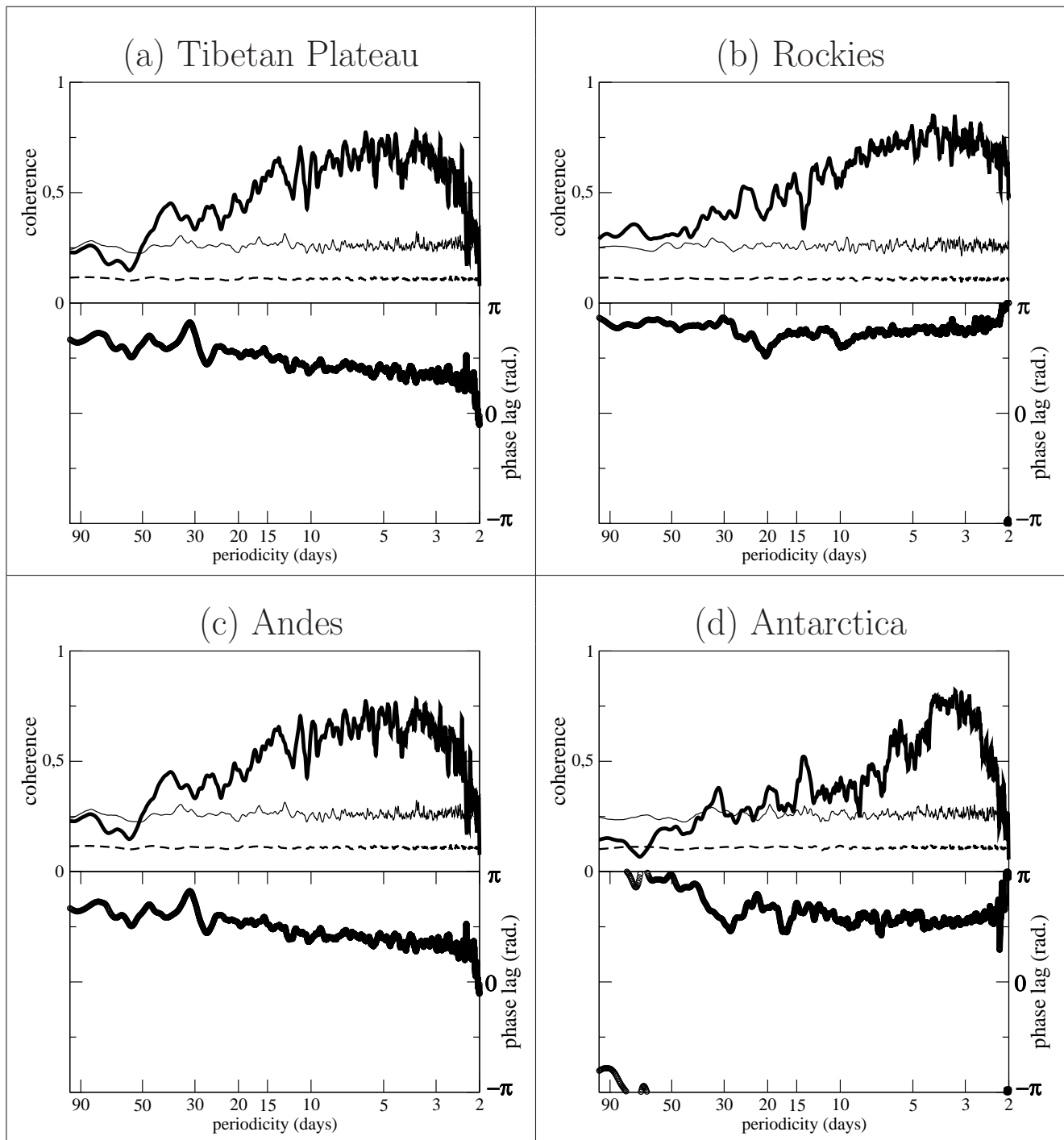


FIG. 3. Coherence and phase relationship between (a) $\tilde{T}_{TP,1}$ and $\tilde{T}_{TP,2}$; (b) $\tilde{T}_{R,1}$ and $\tilde{T}_{R,2}$; (c) $\tilde{T}_{Ad,1}$ and $\tilde{T}_{Ad,2}$; and (d) $\tilde{T}_{At,1}$ and $\tilde{T}_{At,2}$. Same conventions and method as in Fig. 2

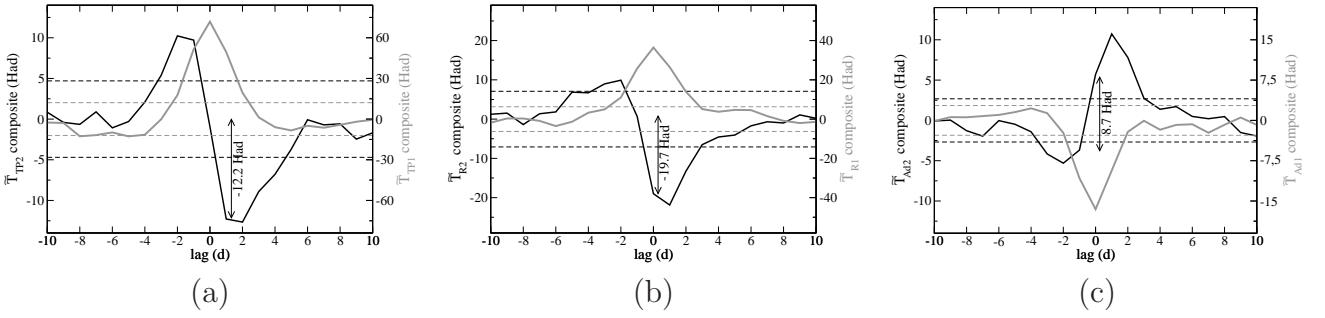


FIG. 4. (a) composite time series of \tilde{T}_{TP1} (gray, solid) \tilde{T}_{TP2} (black, solid) keyed on the 20 strongest positive peaks of \tilde{T}_{TP1} , and corresponding 99% significance levels; (b) same for \tilde{T}_{R1} and \tilde{T}_{R2} keyed on \tilde{T}_{R1} ; and (c) composite time series of \tilde{T}_{Ad1} and \tilde{T}_{Ad2} keyed on the 20 strongest negative peaks of \tilde{T}_{Ad1}

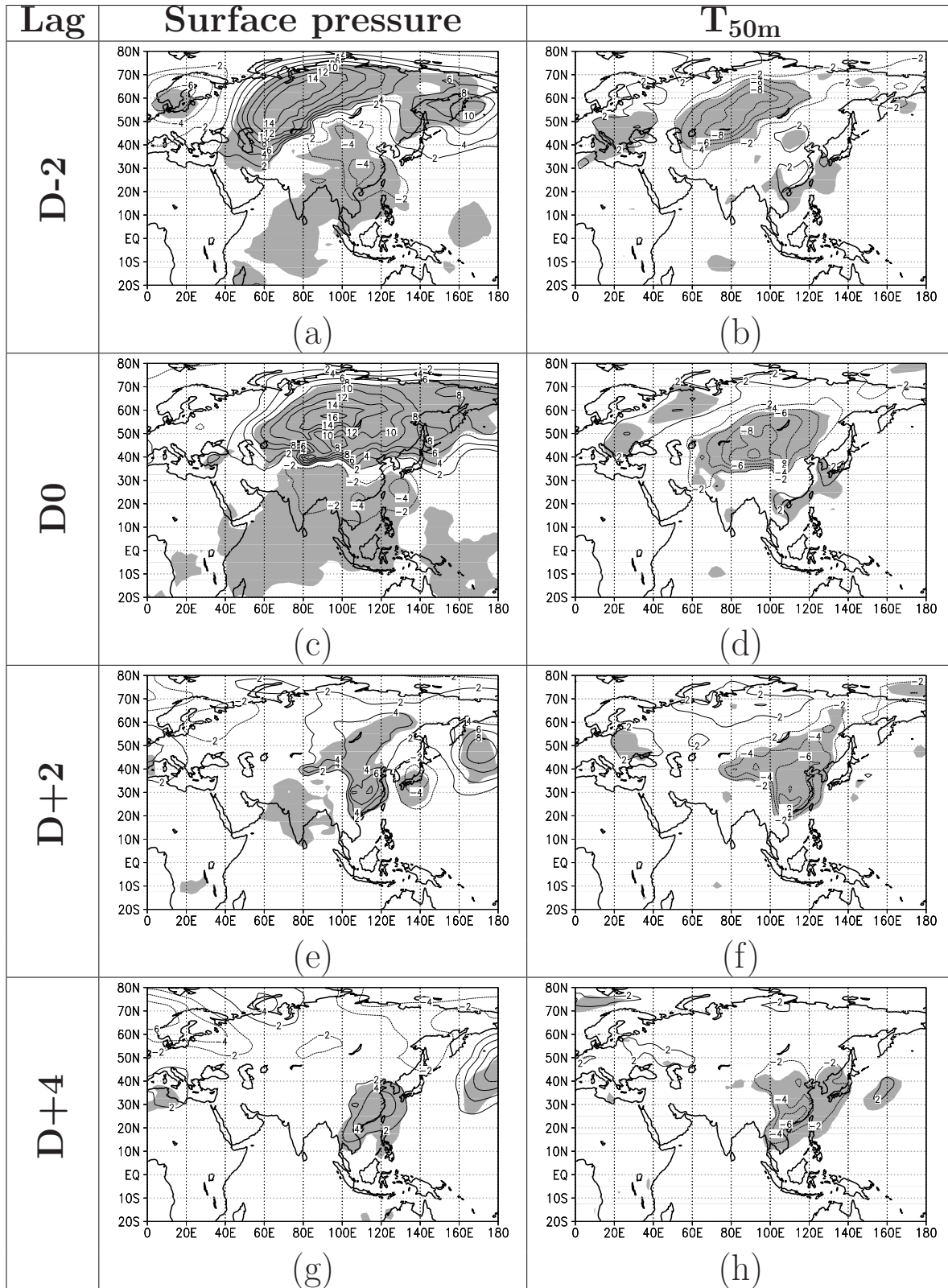


FIG. 5. Composite of the surface pressure anomalies (a,c,e,g) and surface temperature anomalies (b,d,f,h) for the 20 strongest positive peaks of \tilde{T}_{TP1} , at lag D-2 (a,b), D0 (c,d), D+2 (e,f) and D+4 (g,h); 99% confidence level (shaded). Contour interval is 2 hPa for the surface pressures, 2 K for the surface temperatures. Zero-contours are omitted.

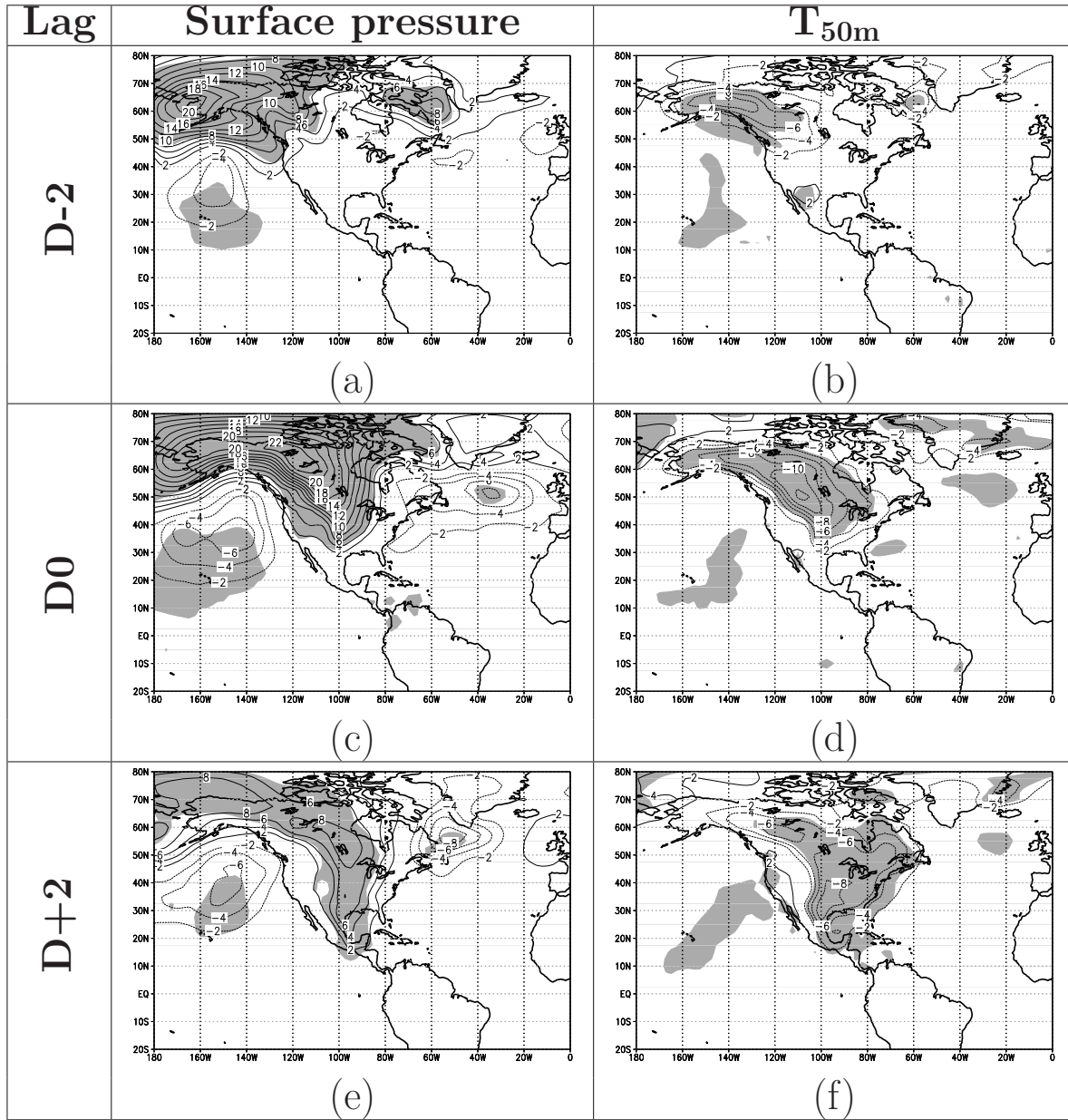


FIG. 6. Same as Fig. 5 but keyed on the positive peaks of \tilde{T}_{R1}

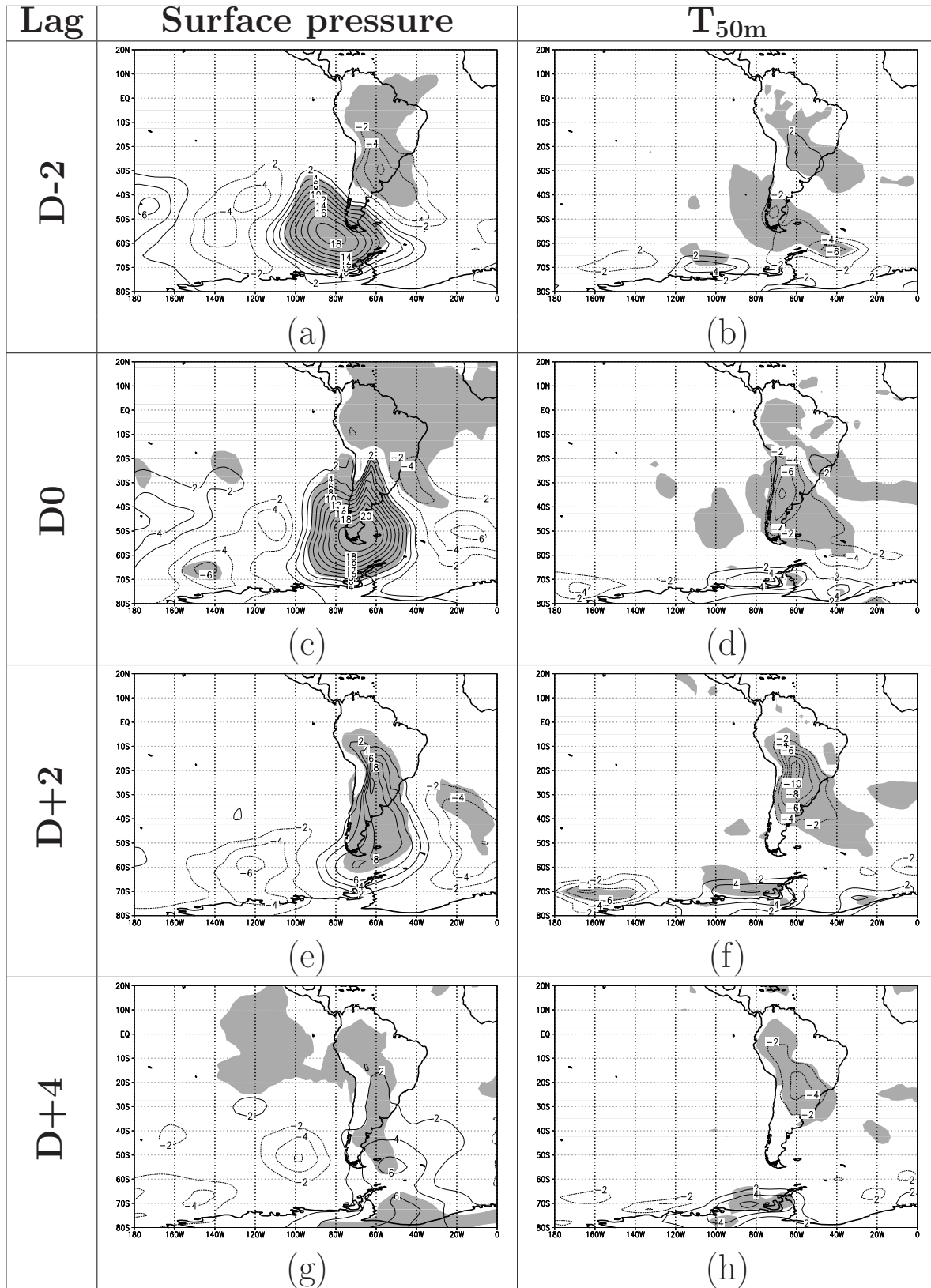


FIG. 7. Same as Fig. 5 but keyed on the negative peaks of \tilde{T}_{Ad1}

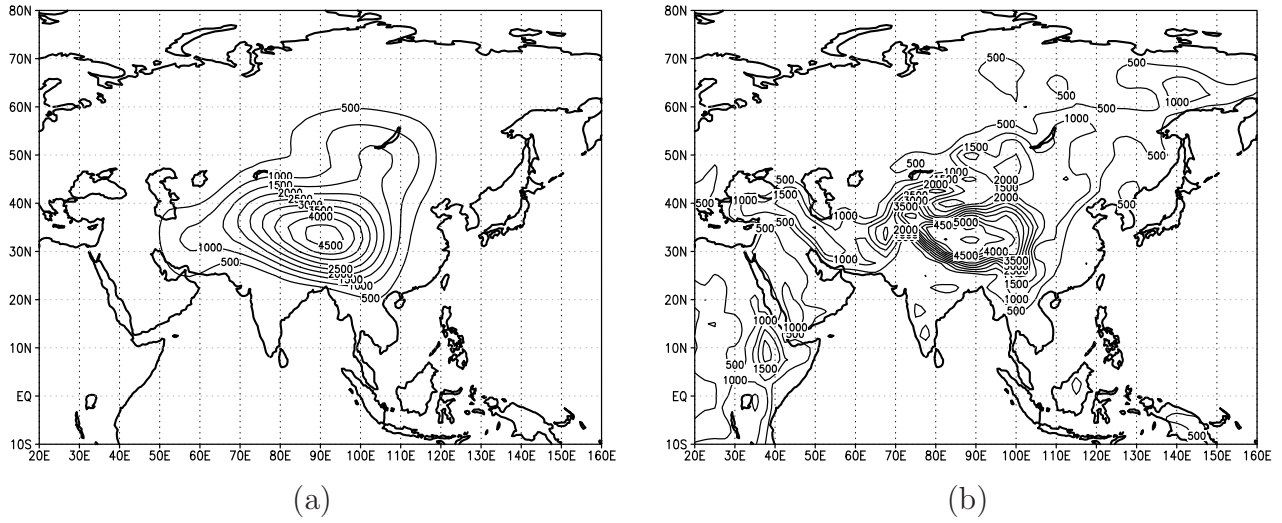


FIG. 8. (a)topography retained for the model run and (b)NCEP topography (meters above sea level). The model topography is obtained by multiplying the T21-filtered NCEP topography by $\alpha(\lambda)\beta(\phi)$, where $\alpha(\lambda)$ (resp. $\beta(\phi)$) is a function whose value is 1 in the interval $[\lambda_1; \lambda_2]$ (resp. $[\phi_1; \phi_2]$) corresponding to the longitude (resp. latitude) range in Table 1; 0 outside $[\lambda_1 - 15^\circ; \lambda_2 + 15^\circ]$ (resp. $[\phi_1 - 15^\circ; \phi_2 + 15^\circ]$); and a smooth connection is ensured by the use of an exponential taper $\varphi(t) = \exp(t^2/(t^2 - 1))$.

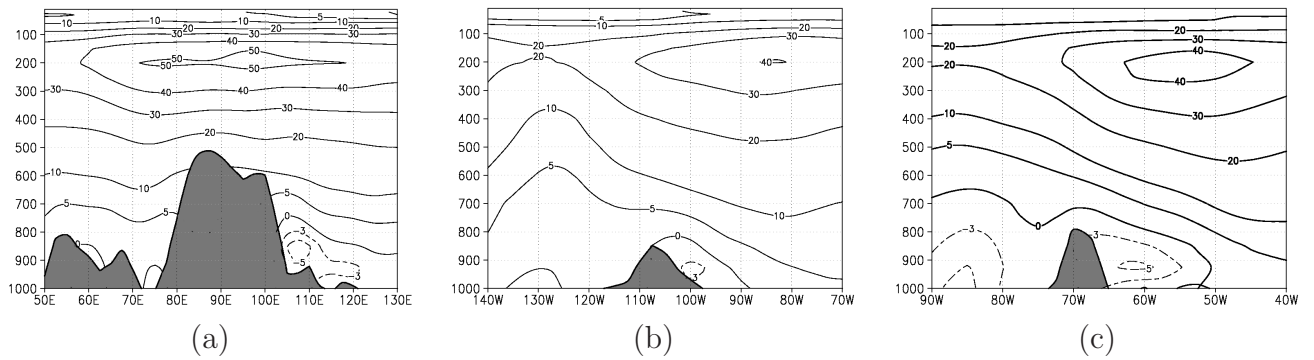


FIG. 9. (a) composite of the zonal wind at 30°N keyed on the 20 strongest positive peaks of $\tilde{T}_{TP,1}$; (b) same as (a) but for the composite keyed on \tilde{T}_{R1} ; (c) composite of the zonal wind at 30°S keyed on the 20 strongest negative peaks of \tilde{T}_{Ad1} . The contours are every 10 ms^{-1} for positive (westerly) winds, at -3 ms^{-1} and -5 ms^{-1} for negative (easterly) winds.

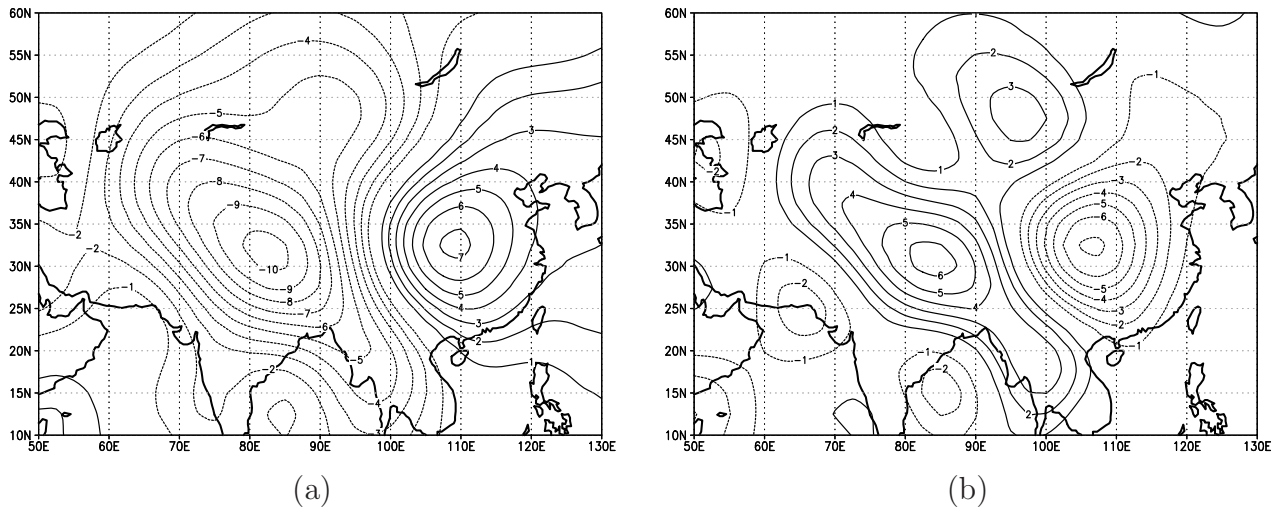


FIG. 10. (a) Sea level pressure tendency between time 0d and time +1d in the model simulation for the Tibetan Plateau (contours every 1 hPa, zero-contour omitted); (b) Surface potential temperature tendency between time 0d and time +1d in the model simulation for the Tibetan Plateau (contours every 1 K, zero-contour omitted)

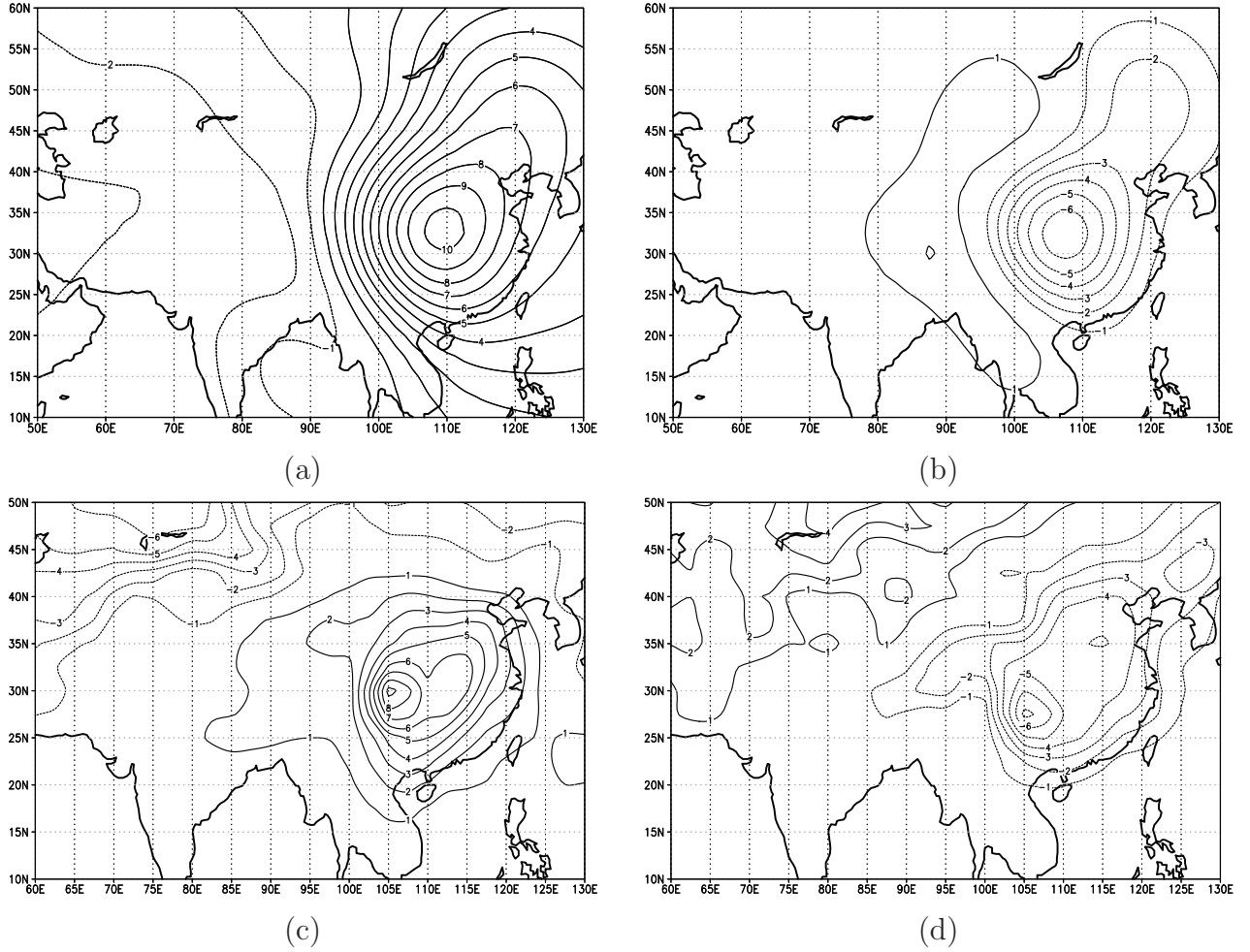


FIG. 11. (a) and (b): same as Fig. 10 but with the modified boundary condition; (c) tendency of \tilde{P}_S between lag 0d and 1d in the composite keyed on the 20 strongest events on \tilde{T}_{TP1} (contours every 1 hPa, zero-contour omitted); (d) tendency of \tilde{T}_{50m} between lag 0d and 1d in the composite keyed on the 20 strongest events on \tilde{T}_{TP1} (contours every 1 K, zero-contour omitted)

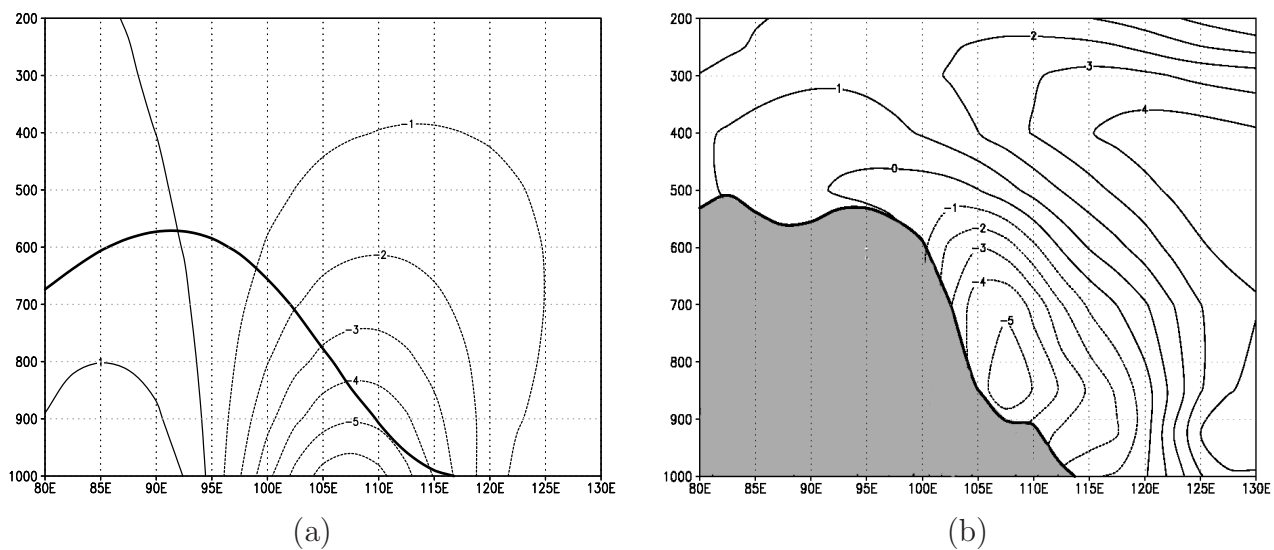


FIG. 12. (a) air temperature anomaly (K, thin contours) at $32.5^\circ N$ at time +1d in the model simulation. The thick black line represents the model ground elevation. (b) composite of air temperature anomaly (relative to the climatology) 1d after after the 20 strongest peaks in \tilde{T}_{TP1}

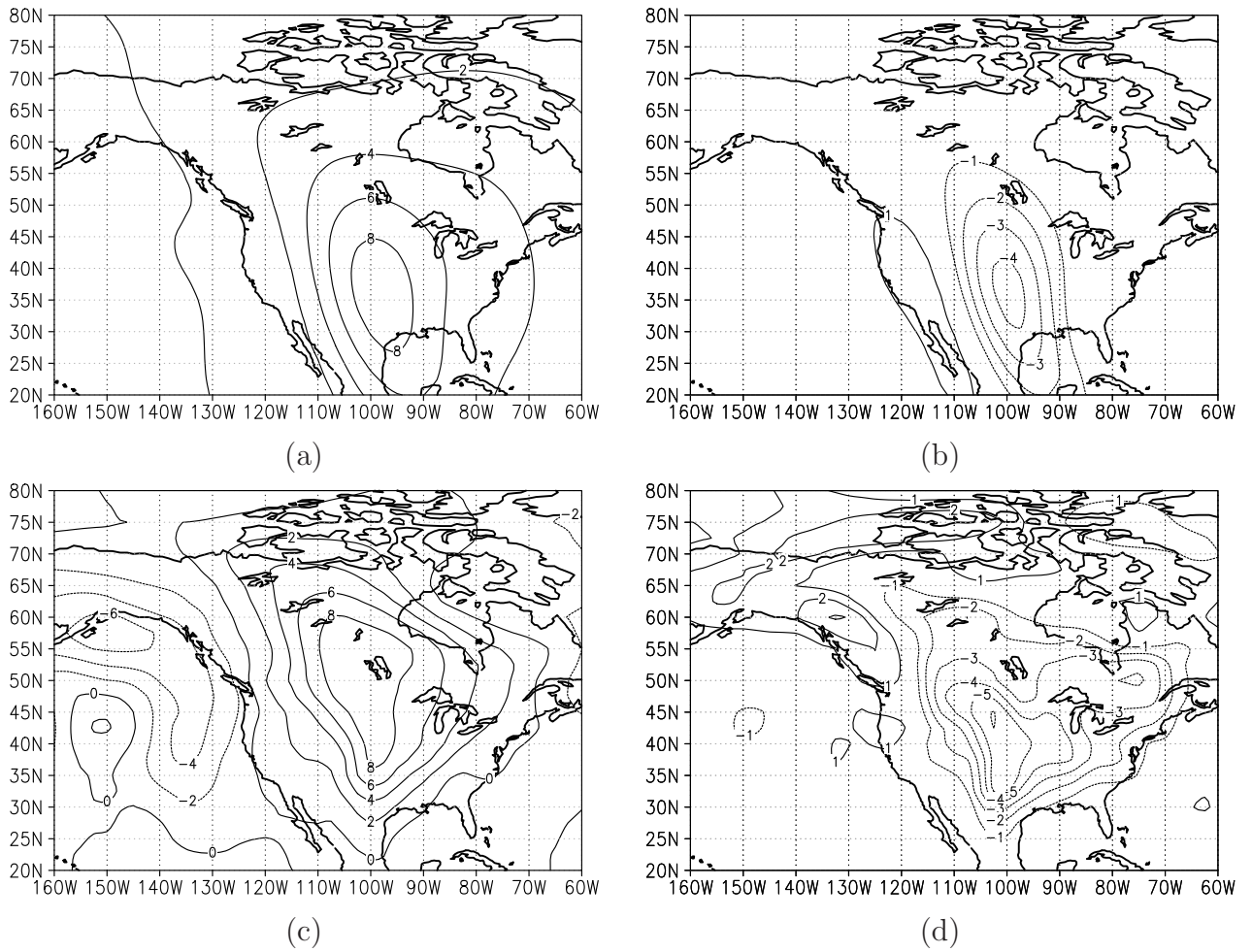
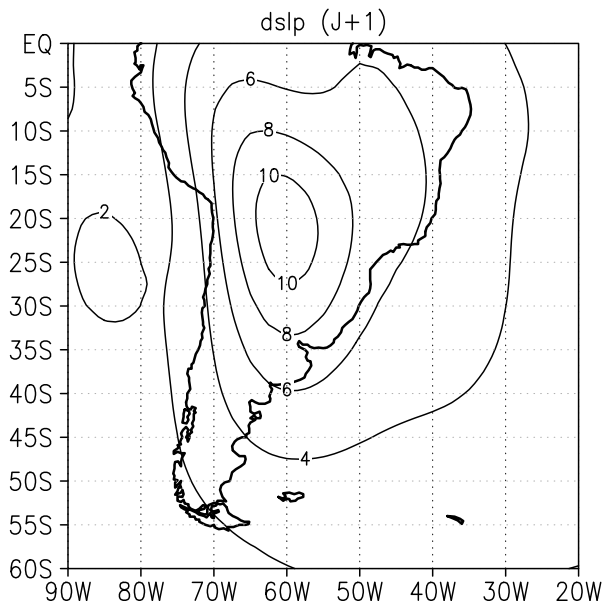
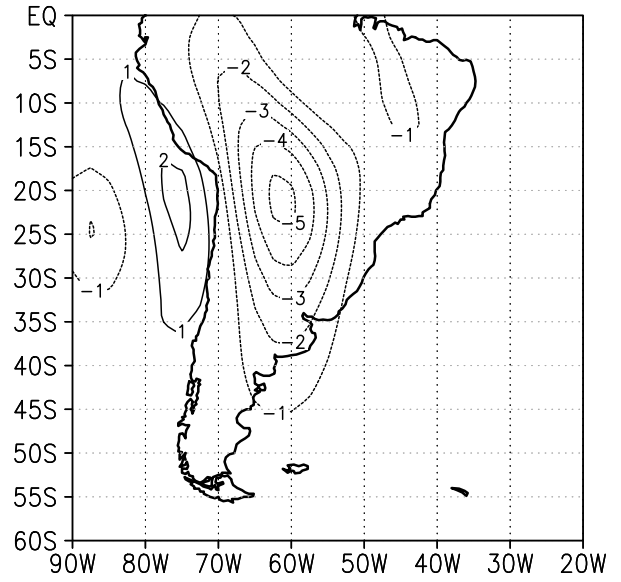


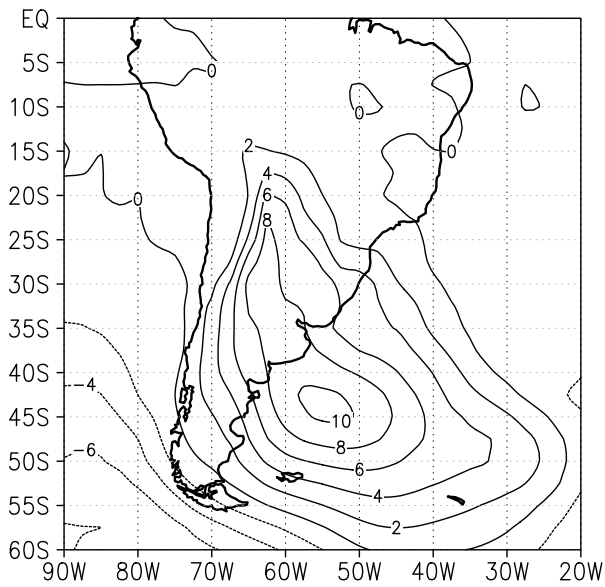
FIG. 13. Same as Fig. 11 but for the Rockies. The 1d differences in (c) and (d) are between the composites at lag 0d and $-1d$



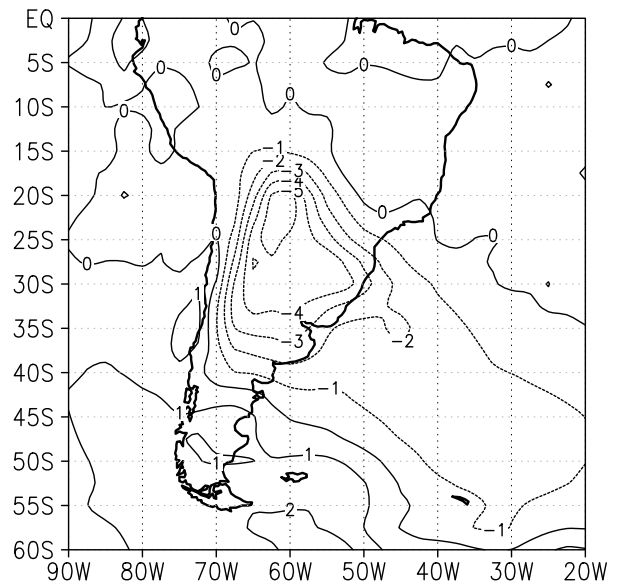
(a)



(b)



(c)



(d)

FIG. 14. Same as Fig. 13 but for the Andes